A Level-Set Method for Magnetic Substance Simulation

XINGYU NI, CFCS, Peking University & AICFVE, Beijing Film Academy
BO ZHU, Dartmouth College
BIN WANG*, AICFVE, Beijing Film Academy
BAOQUAN CHEN*, CFCS, Peking University & AICFVE, Beijing Film Academy

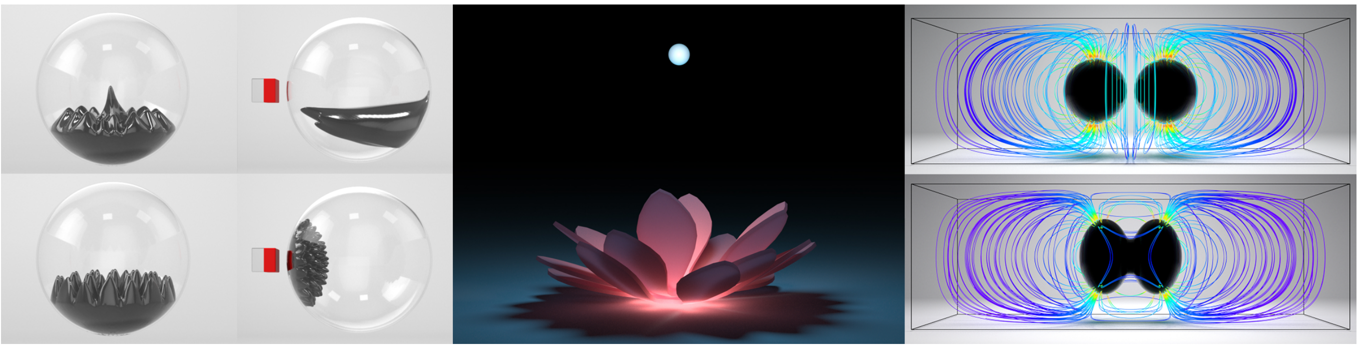

Fig. 1. Our unified level-set based approach can simulate and visualize the dynamics of a broad array of magnetic phenomena including ferrofluids, deformable magnetic bodies, rigid magnetic bodies, and multi-physics interactions.

We present a versatile numerical approach to simulating various magnetic phenomena using a level-set method. At the heart of our method lies a novel two-way coupling mechanism between a magnetic field and a magnetizable mechanical system, which is based on the interfacial Helmholtz force drawn from the Minkowski form of the Maxwell stress tensor. We show that a magnetic-mechanical coupling system can be solved as an interfacial problem, both theoretically and computationally. In particular, we employ a Poisson equation with a jump condition across the interface to model the mechanical-to-magnetic interaction and a Helmholtz force on the free surface to model the magnetic-to-mechanical effects. Our computational framework can be easily integrated into a standard Euler fluid solver, enabling both simulation and visualization of a complex magnetic field and its interaction with immersed magnetizable objects in a large domain. We demonstrate the efficacy of our method through an array of magnetic substance simulations that exhibit rich geometric and dynamic characteristics, encompassing ferrofluid, rigid magnetic body, deformable magnetic body, and multi-phase couplings.

CCS Concepts: • **Computing methodologies** → **Physical simulation**; • **Applied computing** → *Physics.*

*corresponding authors

Authors' addresses: Xingyu Ni, nixy@pku.edu.cn, CFCS, Peking University & AICFVE, Beijing Film Academy; Bo Zhu, bo.zhu@dartmouth.edu, Dartmouth College; Bin Wang, binwangbuaa@gmail.com, AICFVE, Beijing Film Academy; Baoquan Chen, baoquan@pku.edu.cn, CFCS, Peking University & AICFVE, Beijing Film Academy.

0730-0301/2020/7-ART1 $15.00
https://doi.org/10.1145/3386569.3392445

Additional Key Words and Phrases: magnetic simulation, fluid simulation, ferrofluid, level-set method, immersed boundary

ACM Reference Format:
Xingyu Ni, Bo Zhu, Bin Wang, and Baoquan Chen. 2020. A Level-Set Method for Magnetic Substance Simulation. *ACM Trans. Graph.* 39, 4, Article 1 (July 2020), 15 pages. https://doi.org/10.1145/3386569.3392445

1 INTRODUCTION

The coupling between volumetric and interfacial forces acts as the fundamental mechanism for many intricate free-surface flow phenomena that are characterized by visually appealing dynamics and geometries. Among these phenomena, the surface tension flow is the most ubiquitous example, demonstrating the beauty and complexity of such interface-volume interactions. A variety of small-scale features, such as the pinched off droplets [Da et al. 2016a; O'brien and Hodgins 1995; Thürey et al. 2010; Zheng et al. 2015; Zhu et al. 2014], filaments [Bergou et al. 2010], curved thin sheets [Ando and Tsuruno 2011; Batty et al. 2012; Brochu et al. 2012; Da et al. 2014, 2015; Larionov et al. 2017; Saye and Sethian 2013], capillary waves [He et al. 2012; Jeschke and Wojtan 2015a; Saye 2016; Yang et al. 2016], and their co-dimensional combinations [Zhu et al. 2015, 2014], have been captured numerically by the invention of a broad spectrum of computational tools to accommodate the modeling of free-surface flow in computational physics and computer graphics. Among these surface-tension-driven phenomena, magnetic flow exhibits its peculiar surface geometries and dynamics featured by the emergence and evolution of arrays of uniform and sharp cone structures. These appealing features arise due to the multilateral interactions among pressure, surface tension, and magnetic forces.

A natural and immediate question to ask when extending a conventional surface tension solver to model a magnetic flow phenomenon is that, *"Is the magnetic force exerted on a physical substance*

Notation	Name	Definition
$\boldsymbol{H}$	*Magnetic field intensity*	
$\boldsymbol{M}$	*Magnetization intensity*	
$\boldsymbol{B}$	*Magnetic induction intensity*	$\boldsymbol{B} = \mu_0(\boldsymbol{H} + \boldsymbol{M})$
μ_0	*Vacuum permeability*	Constant
$\chi^\dagger$	*Magnetic susceptibility*	
$\mu^\dagger$	*Permeability*	$\mu = (1 + \chi)\mu_0$

† Defined only for linear, isotropic materials.

Table 1. Physical quantities involved in describing a magnetic field.

volumetrically or interfacially?" Astonishingly, this question is yet to be definitely answered, even nowadays, due to the long-disputed *Abraham–Minkowski controversy* that can be traced back to the birth of Maxwell's equations, 150 years ago [Maxwell 1865]. The controversy essentially splits the stream of viewpoints on magnetic force into two main branches by describing the *Maxwell stress tensor* using the *Einstein–Laub form* [Einstein and Laub 1908] and the *Minkowski form* [Minkowski 1908].

1.1 Mathematical motivation

Here we briefly review some formulae as a high-level introduction to the mathematical foundations of our approach. Intuitive explanation and detailed derivation can be found in Appendix A.1. Table 1 lists physical quantities involved in describing a magnetic field. In essence, the electromagnetic theory studies the interactions among three fields — *magnetic field intensity* $\boldsymbol{H}$, *magnetization intensity* $\boldsymbol{M}$ and *magnetic induction intensity* $\boldsymbol{B}$. The mechanical effect of these magnetic interactions is measured by the Maxwell stress tensor in vacuum, denoted $\boldsymbol{T}_m$, which can be written as

$$\boldsymbol{T}_\mathrm{m} = \frac{1}{\mu_0}\left(\boldsymbol{B} \otimes \boldsymbol{B} - \frac{1}{2}B^2\boldsymbol{I}\right) \tag{1}$$

with μ_0 as the constant *vacuum permeability* and the electric terms omitted. This form is the root of both the Einstein–Laub form and the Minkowski form in matter. The Einstein–Laub form of the Maxwell stress tensor and its divergence (known as the *Kelvin force*) are

$$\boldsymbol{T}_\mathrm{m}^\mathrm{E} = \boldsymbol{B} \otimes \boldsymbol{H} - \frac{\mu_0}{2}H^2\boldsymbol{I}, \tag{2}$$

$$\boldsymbol{f}_\mathrm{m}^\mathrm{E} = \nabla \cdot \boldsymbol{T}_\mathrm{m}^\mathrm{E} = \mu_0\boldsymbol{M} \cdot \nabla\boldsymbol{H}, \tag{3}$$

On the other hand, the Minkowski form and its corresponding force term (known as the *Helmholtz force*) have the formulae as

$$\boldsymbol{T}_\mathrm{m}^\mathrm{M} = \boldsymbol{B} \otimes \boldsymbol{H} - \frac{1}{2}(\boldsymbol{B} \cdot \boldsymbol{H})\boldsymbol{I}, \tag{4}$$

$$\boldsymbol{f}_\mathrm{m}^\mathrm{M} = \nabla \cdot \boldsymbol{T}_\mathrm{m}^\mathrm{M} = \boldsymbol{B} \cdot \nabla\boldsymbol{H} - \frac{1}{2}\nabla(\boldsymbol{B} \cdot \boldsymbol{H}). \tag{5}$$

By making assumptions of linearity and isotropy of the magnetic substances, which apply to most cases of the macroscopic magnetic phenomena [Ishikawa et al. 2013; Kim et al. 2018; Thomaszewski et al. 2008], the Kelvin force in Equation (3) and the Helmholtz force in Equation (5) can be further simplified as

$$\boldsymbol{f}_\mathrm{m}^\mathrm{E} = \frac{\mu_0}{2}\chi\nabla\left(H^2\right), \tag{6}$$

$$\boldsymbol{f}_\mathrm{m}^\mathrm{M} = -\frac{\mu_0}{2}H^2\nabla\chi, \tag{7}$$

with χ as the *magnetic susceptibility*, which amounts to material trackers to distinguish different substances (zero in vacuum).

Interfacial Helmholtz force. We can make two immediate observations from Equation (6) and Equation (7) that motivate the design of our numerical approach for unified magnetic substance simulation. First, **the Kelvin force is volumetric, while the Helmholtz force is interfacial**. This mathematical fact is evidenced by the non-zero $\nabla\left(H^2\right)$ over the entire space for the Kelvin term and the non-zero $\nabla\chi$ on the interface only for the Helmholtz term (by considering χ as a Heaviside function distinguishing the vacuum and the magnetic substance volume). From a numerical perspective, the volumetric Kelvin force with a non-zero bulk distribution is well suited for a Lagrangian approach (e.g., SPH particles [Huang et al. 2019]) while the interfacial Helmholtz force with a surface concentration can be adopted into an Eulerian framework with interface treatments. Second, **the Kelvin force and the Helmholtz force are mathematically equivalent** if a physical system undergoing magnetic interactions consists of a hydro-static stress term with appropriate Dirichlet boundary conditions on the free surface (e.g., pressure for incompressible interfacial flow). This fact can be demonstrated straightforwardly by subtracting Equation (7) from Equation (6) to get

$$\Delta\boldsymbol{f}_\mathrm{m} = \boldsymbol{f}_\mathrm{m}^\mathrm{E} - \boldsymbol{f}_\mathrm{m}^\mathrm{M} = \nabla\left(\frac{\chi\mu_0 H^2}{2}\right), \tag{8}$$

which shows that the difference between the Kelvin and Helmholtz forces can be modeled as the gradient of a potential field Φ. Specifically, if the ordered pair $\left(\boldsymbol{f}_\mathrm{m}^\mathrm{E}, p\right)$ is a quasi-static solution of magnetic force and pressure, $\left(\boldsymbol{f}_\mathrm{m}^\mathrm{M}, p - \Phi\right)$ must be another valid solution, because 1) $\boldsymbol{f}_\mathrm{m}^\mathrm{E} - \nabla p = \boldsymbol{f}_\mathrm{m}^\mathrm{M} - \nabla(p - \Phi)$ (the total force leaves the same); and 2) $p = p - \Phi = 0$ in vacuum (satisfying the same boundary condition). In a numerical sense, this magnetic potential gradient can be absorbed to the pressure gradient (e.g., during the projection step of a conventional Euler solver [Fedkiw et al. 2001]), opening up possibilities to creating fast numerical simulators by leveraging the existing high-performance Poisson solvers on a Cartesian grid.

1.2 Numerical approach

Motivated by the above two mathematical observations for the Helmholtz force, we design a novel, unified level-set based approach to model the dynamics of a broad array of magnetic substances, ranging from fluids and rigid bodies, to soft bodies and their multilateral couplings. Our essential contribution is numerically modeling the volumetric magnetic-mechanical coupling problem by solving an interfacial flow problem. By considering a dynamic system, either Lagrangian or Eulerian, immersed in an Eulerian magnetic field, we establish an effective numerical method to treat their two-way interactions empowered by the interfacial Helmholtz force and the immersed moving materials simultaneously. In particular, this mechanical-magnetic two-way coupling is devised in a codimensional fashion. The forward coupling from the magnetic field to the mechanical system is interfacial, by modeling the surface effect of the Helmholtz force on a moving object (e.g., fluid or solid), while the backward coupling from physical system to the magnetic field is volumetric, by tracking the moving magnetic materials (level-set, particles, or mesh) immersed in a background magnetic field. From a physical perspective, this coupling mechanism is fundamentally different from those conventional FSI or multi-phase fluids solvers, in which case the interfacial stress acts as the sole medium to enforce the interactions. From a numerical perspective, however, this scheme shares nontrivial common threads with the various weakly coupling approaches, e.g., the immersed boundary methods [Peskin 1972], by solving the evolution of a magnetic field on a background Eulerian grid and restricting the interaction on a high-codimensional interface.

Compared with its particle counterparts, our proposed level-set approach demonstrates its unique merits in (1) modeling magnetic phenomena regarding computational efficiency and scalability by restricting the magnetic-to-mechanical interactions on the surface only, (2) the ease for code implementation by extending an Eulerian simulator with one additional Poisson solve, and most importantly, (3) the seamless integration into the modern industrial pipelines for visual fluid simulation and its multi-physics couplings by treating other simulators simply as black boxes. On the scientific side, thanks to the Eulerian nature of our approach, the proposed level-set method inherently enables the accurate calculation of long-range magnetic interactions regardless of the distance between the immersed objects. Moreover, a precise visualization of the magnetic streamlines distributed in a large open space can be obtained without requiring any additional computational resources. This scientific computing framework bridges the communities of high-performance computing, computer graphics, and scientific data visualization by enabling the effective exploration and illustration of complex magnetic phenomena.

Contributions. We summarize our main contributions as follows:

- The first versatile level-set approach to modeling a broad range of magnetic phenomena including fluids, solids, and their couplings in a unified way,
- A novel computational approach based on the interfacial Helmholtz force model to solve the magnetic-mechanical coupling problem as an immersed boundary problem,
- An efficient numerical scheme to model the magnetic phenomena by solving a Poisson equation with jump conditions that can be incorporated into a standard Euler fluid solver.

2 RELATED WORK

Magnetic substance simulation. Beginning with the pioneering work of [Oldenburg et al. 2000], a surge of literature has been devoted to the development of Eulerian numerical schemes to simulate ferrofluid in a computational physics setting. To simulate the spike structure of ferrofluid, some works make use of the finite element method (FEM) with Kelvin force [Cao and Ding 2014; Gollwitzer et al. 2007; Yoshikawa et al. 2011]. Due to the computational cost, such methods cannot deal with dynamics well and are not easy to generalize to other magnetic phenomena. The Helmholtz force perspective has been investigated through the development of several numerical schemes for modeling engineering-ferrofluid, including the particle level-set [Liu et al. 2011] and the volume of fluid [Ghaffari et al. 2015; Shi et al. 2014]. However, none of these approaches are able to provide an efficient, scalable algorithm to capture the intricate 3D surface geometries. In the visual computing community, the Kelvin point of view dominates the literature. For example, [Ishikawa et al. 2013] employs a smoothed-particle hydrodynamics (SPH) approach to simulating ferrofluid by treating each particle as a magnetic dipole. A procedural method is devised to generate the spike structure on the surface. [Huang et al. 2019] invents an accurate large-scale SPH simulation scheme by incorporating the fast multipole method (FMM) into the Lagrangian framework to model the magnetic evolution, which produces visually captivating effects and demonstrates the state-of-the-art performance by scaling up to millions of particles. Besides magnetic fluids, the previous literature is devoted to the numerical modeling of magnetic solids (e.g., see [Thomaszewski et al. 2008], [Kim et al. 2018], [Zhao et al. 2019]), which also follows the Kelvin assumption owing to their Lagrangian nature.

Interfacial flow simulation. Beginning with the pioneering work of [Foster and Fedkiw 2001], a vast literature has been devoted to simulating the various kinds of flow phenomena with its evolution defined by a sharp interface in computer graphics. A broad spectrum of interfacial effects, such as foam and spray [Losasso et al. 2008], waves [Jeschke et al. 2018; Jeschke and Wojtan 2015b, 2017; Schreck et al. 2019], surface tension [Ando and Tsuruno 2011; Da et al. 2014, 2015; Saye and Sethian 2013; Zhu et al. 2015, 2014] , chemical reaction [Nguyen et al. 2003, 2002], multi-phase flow [Losasso et al. 2006b; Solenthaler and Gross 2011], viscous coiling [Batty and Bridson 2008], etc., have been reproduced in a computational setting by the invention of many high-performance numerical simulators. Underlying these visually appealing simulations, the level-set approach [Osher and Fedkiw 2005] and the particle approach are the two mainstream techniques that demonstrate their incomparable effectiveness in capturing the complex dynamics and geometry of an evolving interface. The level-set method tracks the interface by evolving a signed distance field on an Eulerian background discretization (e.g., a uniform grid), which allows the generation of highly complicated topological changes and geometrical evolutions of an implicit surface [Hong et al. 2007; Kim et al. 2013; Losasso et al. 2006a; Zheng et al. 2015]. The Eulerian nature of the interface enables the usage of a variety of acceleration structures, such as an Octree [Losasso et al. 2004] or a sparsely populated grid [Aanjaneya et al. 2017; Liu et al. 2018; Setaluri et al. 2014], and a bank of high-performance parallel solvers [Liu et al. 2016] to boost the performance of the simulation. On another front, particle approaches, as well as their various hybrid grid-particle variations, demonstrate their efficacy in capturing the various material properties, such as granular [Jiang et al. 2019; Yue et al. 2018; Zhu and Bridson 2005], plastoelastic [Fang et al. 2019; Gao et al. 2017; Jiang et al. 2017; Klár et al. 2016], foam [Ram et al. 2015; Yue et al. 2015] and non-Newtonian materials [Zhu et al. 2015], and coupling effects [Fei et al. 2018, 2019, 2017] that were challenging for a conventional grid-based method.

3 PHYSICAL MODELS

3.1 Magnetic-Material Interaction Overview

Four-step interaction. The magnetic interaction process between a background magnetic field and a magnetic substance consists of four steps — **magnetization**, **induction**, **exertion**, and **reshaping** — which guide the design of our computational pipeline. Here we

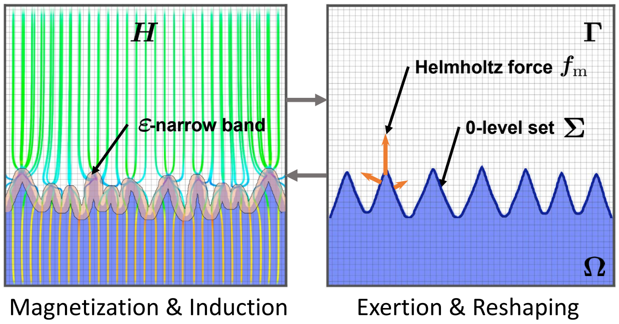

Fig. 2. Algorithm overview. Our framework consists of four steps: magnetization, induction (left), exertion, and reshaping (right). The coupling happens on a level-set interface on both the magnetic and mechanical sides.

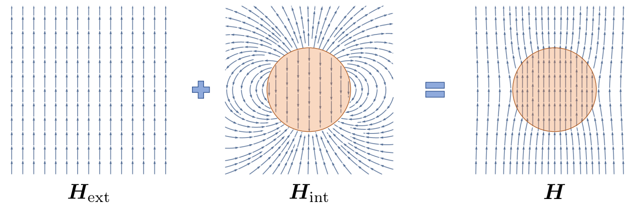

Fig. 3. An example of magnetization and induction. A sphere in a uniform magnetic field ($\boldsymbol{H}_{ext}$) is magnetized and produces an induced field ($\boldsymbol{H}_{int}$), which will further lead to a synthesized field ($\boldsymbol{H}$).

briefly introduce these four steps on a high level of understanding. Please refer to Appendix A.2 for a microscopic interpretation of **magnetization** and **induction**. First, in the **magnetization** step, the external magnetic field $\boldsymbol{H}_{ext}$ magnetizes the immersed magnetic substance according to its current shape and position. Second, in the **induction** step, the magnetized substance further induces an internal magnetic field $\boldsymbol{H}_{int}$, which is then linearly combined with the existing external magnetic field, i.e., $\boldsymbol{H} = \boldsymbol{H}_{ext} + \boldsymbol{H}_{int}$ (see Figure 3), to apply a magnetic forces $\boldsymbol{f}_m$ on the subject in the **exertion** step. Last, in the **reshaping** step, the state of the physical system is updated according to the exerted magnetic force, which in turn affects the magnetization step by intriguing a new $\boldsymbol{H}_{int}$ and closing the loop of coupling. Take Figure 2 as a reference.

Naming convention. We symbolize vectors and second-order tensors using bold letters (such as $\boldsymbol{H}$ and $\boldsymbol{T}$) and symbolize scalars using italic letters (such as H and μ). In particular, if a bold letter is used to stand for a vector, the corresponding italic letter will symbolize the same quantity, omitting information of directions (e.g., $H = |\boldsymbol{H}|$). Since the Helmholtz formula of the magnetic force is adopted, for annotation conciseness we will start to use $\boldsymbol{f}_m$ (instead of $\boldsymbol{f}_m^M$) to denote the Helmholtz force in the rest of the paper (except Appendix A.1).

Magnetic-material coupling. We model the interaction between a magnetic substance (e.g., ferrofluid) and a background magnetic field in the world space Γ. The domain of the magnetic object is denoted by Ω with its boundary Σ (see Figure 2). We use an indicator function I_Ω to define the motion of Ω immersed in Γ:

$$I_\Omega(\boldsymbol{r}) = \begin{cases} 1, & \boldsymbol{r} \in \Omega, \\ 1/2, & \boldsymbol{r} \in \Sigma, \\ 0, & \boldsymbol{r} \in \Gamma \setminus (\Omega \cup \Sigma), \end{cases} \tag{9}$$

with $\boldsymbol{r}$ as a position in the world space. The co-evolution of the induced magnetic field and the material dynamics is coupled by a set of partial differential equations governing the dynamics of the fields for magnetic effects ($\boldsymbol{H}, \boldsymbol{B}, \boldsymbol{M}$) and the fields for moving materials ($\boldsymbol{u}, p, \boldsymbol{\sigma}, I_\Omega$), which can be summarized on a high level as:

$$\begin{cases} M(\boldsymbol{H}, \boldsymbol{B}, \boldsymbol{M}, I_\Omega) = 0 & \text{in } \Gamma, \quad (10a) \\ F(\boldsymbol{u}, p, \boldsymbol{\sigma}, I_\Omega, \boldsymbol{f}_m(H)) = 0 & \text{in } \Omega \cup \Sigma. \quad (10b) \end{cases}$$

The first set of equations describe the evolution of the background magnetic field. The second set of equation(s) denote the dynamics of the immersed magnetic material under the influence of the Helmholtz boundary effects. In particular, the magnetic evolution is instantiated by Maxwell's equations under the magnetostatic assumption (see Section 3.2) that is solved in the entire domain Γ. The material dynamics is exemplified by different physical systems, such as the Navier-Stokes equations for fluids, elastic equations for soft bodies, rigid-body dynamics, or their multi-phase couplings (see Section 3.3). The material domain of Ω is tracked in either an Eulerian or a Lagrangian fashion. The two-way coupling is realized by the evolving I_Ω in the magnetic equations (from magnetics to dynamics) and the immersed boundary Helmholtz force on Σ in the dynamic equations (from dynamics to magnetics).

3.2 Magnetic Field Evolution

The evolution of a magnetic field is governed by Maxwell's equations

$$\begin{cases} \nabla \cdot \boldsymbol{B} = 0, & (11a) \\ \nabla \times \boldsymbol{H} = \boldsymbol{j}_f + \dfrac{\partial \boldsymbol{D}}{\partial t}. & (11b) \end{cases}$$

Here $\boldsymbol{j}_f$ is the *electric current density* of free charges and $\boldsymbol{D}$ is the *electric displacement field* affecting the magnetic field by electromagnetic induction. For (nearly) non-conductive magnetic objects, such as ferrofluid, we can assume steady-state electric displacement $\partial \boldsymbol{D}/\partial t = 0$ and zero free current, $\boldsymbol{j}_f = 0$, inside and on the boundary of the object.

The magnetic and the material fields satisfy the following four relations:

$$\begin{cases} \boldsymbol{H} = \boldsymbol{H}_{ext} + \boldsymbol{H}_{int}, & (12a) \\ \boldsymbol{B} = \mu_0(\boldsymbol{H} + \boldsymbol{M}), & (12b) \\ \boldsymbol{M} = \chi \boldsymbol{H}, & (12c) \\ \chi = k I_\Omega, & (12d) \end{cases}$$

where Equation (12b) is the definition of $\boldsymbol{B}$ and Equation (12c) is the relation between $\boldsymbol{M}$ and $\boldsymbol{H}$ for linear, isotropic materials. Equation (12d) assigns different susceptibility values to each domain, with k as the one in Ω. Physicists also define the *permeability* as

$$\mu = \mu(\boldsymbol{r}) = (1 + \chi(\boldsymbol{r}))\mu_0 \tag{13}$$

in order to simplify Equation (12b) to

$$\boldsymbol{B} = \mu \boldsymbol{H}. \tag{14}$$

Considering the fact that Maxwell's equation is ubiquitously true for both the external magnetic field $\boldsymbol{H}_{ext}$ and the total magnetic field $\boldsymbol{H}_{\text{ext}} + \boldsymbol{H}_{\text{int}}$, we can substitute $\hat{\boldsymbol{H}}_1 = \boldsymbol{H}_{\text{ext}}$ and $\hat{\boldsymbol{H}}_2 = \boldsymbol{H}_{\text{ext}} + \boldsymbol{H}_{\text{int}}$ into Equation (11) in separate and perform subtraction to obtain:

$$\begin{cases} \nabla \cdot (1+\chi)\boldsymbol{H}_{\text{int}} = -\nabla \cdot \chi \boldsymbol{H}_{\text{ext}}, & (15a) \\ \nabla \times \boldsymbol{H}_{\text{int}} = 0. & (15b) \end{cases}$$

According to Equation (15b), $\boldsymbol{H}_{\text{int}}$ is conservative. Therefore, we can let $\boldsymbol{H}_{\text{int}} = -\nabla\psi$, with ψ as a potential function, which can be further substituted into Equation (15a) to get a Poisson's equation with varying coefficients for ψ:

$$\nabla \cdot (1+\chi)\nabla\psi = \nabla \cdot \chi \boldsymbol{H}_{\text{ext}}. \tag{16}$$

Theoretically, to solve Equation (15), a boundary condition that $\psi \to 0, |\boldsymbol{r}| \to \infty$ is involved. It is noteworthy that the solution for Equation (16) exhibits a C^0 continuity over the domain of Γ with a discontinuous derivative across Σ. This gradient discontinuity leads to a discontinuous $\boldsymbol{H}_{\text{int}}$ across Σ with an undefined value on the interface. After solving Equation (16), the total magnetic field can be obtained by

$$\boldsymbol{H} = \boldsymbol{H}_{\text{ext}} - \nabla\psi. \tag{17}$$

Helmholtz force. The jump of $\boldsymbol{H}_{\text{int}}$ across the interface further results in an interfacial Helmholtz force (Equation (7)) applied on the boundary of the magnetic material. Here we briefly show the formula of the interfacial Helmholtz force. We refer the readers to Section 4.1 and Appendix A.3 for a more rigorous proof. By exploiting the property of the indicator function defined in Equation (9) that

$$\nabla I_\Omega(\boldsymbol{r}) = -\delta_\Sigma(\boldsymbol{r})\hat{\boldsymbol{n}}(\boldsymbol{r}), \tag{18}$$

where $\delta_\Sigma(\boldsymbol{r})$ is the generalized *Dirac delta function*, with infinite value on Σ and 0 everywhere else, and $\hat{\boldsymbol{n}}$ is the unit normal pointing outwards Ω of the interface, we can substitute Equation (12d) into Equation (7) and then rewrite the expression of $\boldsymbol{f}_{\text{m}}$ as

$$\boldsymbol{f}_{\text{m}} = \frac{\mu_0}{2} k H^2 \delta_\Sigma(\boldsymbol{r})\hat{\boldsymbol{n}}, \tag{19}$$

which indicates the fact that the Helmholtz force is exerted on the interface only. However, because of undefined $\boldsymbol{H}$ on the interface, we must further take the weak form of the Dirac delta function and supplement the definition of $\boldsymbol{H}$ in order to obtain a well-defined formula that

$$\boldsymbol{f}_{\text{m}} = \frac{\mu_0}{2} k \left[H^2 + \frac{k^2}{4k+4} (\boldsymbol{H} \cdot \hat{\boldsymbol{n}})^2 \right] \delta_\Sigma(\boldsymbol{r})\hat{\boldsymbol{n}}. \tag{20}$$

Here, $\boldsymbol{H}$ on the interface is a weighted average value over the discontinuity:

$$\boldsymbol{H} = \frac{\mu_1 \boldsymbol{H}_1 + \mu_2 \boldsymbol{H}_2}{\mu_1 + \mu_2} \tag{21}$$

with $\mu_1 = (1+k)\mu_0$, $\mu_2 = \mu_0$, $\boldsymbol{H}_1$ measured on the inner interface and $\boldsymbol{H}_2$ measured on the outer interface. This interfacial force can be applied to different mechanical systems to enable the magnetic-mechanical coupling effects in different model settings.

3.3 Magnetic Substance Evolution

Three material models are presented in order to instantiate Equation (10b) in the coupling model under the influence of a background magnetic field. These models include incompressible ferrofluid, magnetic soft body and magnetic rigid body.

Incompressible ferrofluid. We consider the Navier-Stokes equations with an additional interfacial Helmholtz force term as:

$$\begin{cases} \rho \left(\dfrac{\partial \boldsymbol{u}}{\partial t} + \boldsymbol{u} \cdot \nabla \boldsymbol{u} \right) = -\nabla p + \rho \nu \nabla^2 \boldsymbol{u} + \rho \boldsymbol{g} + \boldsymbol{f}_{\text{c}} + \boldsymbol{f}_{\text{m}}, & (22a) \\ \nabla \cdot \boldsymbol{u} = 0. & (22b) \end{cases}$$

with t as time, $\boldsymbol{u}$ as the velocity, p as the pressure, ρ as the mass density, ν as the *kinematic viscosity*, $\boldsymbol{g}$ as the gravity, and $\boldsymbol{f}_c$ as the surface tension. In particular, the surface tension is defined as $\boldsymbol{f}_{\text{c}} = -\sigma\kappa\hat{\boldsymbol{n}}$ with σ as the surface tension coefficient and κ as the *mean curvature.*

Magnetic elastic body. We consider the Lagrangian formula of the elastic equation under the influence of a magnetic field as an additional boundary coupling by Helmholtz force as

$$\rho \left(\frac{\partial \boldsymbol{u}}{\partial t} + \boldsymbol{u} \cdot \nabla \boldsymbol{u} \right) = \nabla \cdot \boldsymbol{\sigma} + \rho \boldsymbol{g} + \boldsymbol{f}_{\text{m}}, \tag{23}$$

with $\boldsymbol{\sigma}$ as the *elastic stress.*

Magnetic rigid body. We consider the Euler equation to model the magnetic rigid body dynamics that is immersed in a magnetic field, with a boundary integral term for the effects of the Helmholtz force as

$$\begin{cases} m_\rho \dfrac{\mathrm{d}\boldsymbol{u}}{\mathrm{d}t} = m_\rho \boldsymbol{g} + \oiiint_\Omega \boldsymbol{f}_{\text{m}} \, \mathrm{d}V, & (24a) \\ \boldsymbol{I}_\rho \dfrac{\mathrm{D}\boldsymbol{\omega}}{\mathrm{D}t} + \boldsymbol{\omega} \times (\boldsymbol{I}_\rho \cdot \boldsymbol{\omega}) = \oiiint_\Omega (\boldsymbol{d} \times \boldsymbol{f}_{\text{m}}) \, \mathrm{d}V, & (24b) \end{cases}$$

with m_ρ as the mass, $\boldsymbol{I}_\rho$ as the inertia tensor (relative to the center of mass), $\mathrm{D}(\cdot)/\mathrm{D}t$ as the derivative in a body-fixed frame of reference, $\boldsymbol{\omega}$ as the angular velocity, and $\boldsymbol{d}$ as the vector from the center of mass to an object point.

Multi-physics coupling. For liquid-liquid coupling, i.e., the multiphase flow, the Helmholtz force is exerted on the two-phase interface instead of the liquid surface. For solid-liquid coupling, there is a boundary condition $(\boldsymbol{u} - \boldsymbol{u}_{\text{solid}}) \cdot \hat{\boldsymbol{n}} = 0$ involved, and the entire system must follow the laws of conservation of momentum and energy. In these cases, the value of χ needn't follow Equation (12d) and each material can have its own susceptibility. Despite this, in the text of this paper, we still define I_Ω and assume $\chi = kI_\Omega$ for simplicity.

4 NUMERICAL ALGORITHMS

We present our numerical model to solve the coupled magnetic-material equations discussed in the previous section. The magnetic field is discretized on a Cartersian MAC grid [Harlow and Welch 1965]. The scalar fields (e.g., ψ) are stored on cell centers and the vector fields (e.g., $\boldsymbol{H}$) are stored on faces. The material evolution is modeled using a level-set signed distance field, which functions as two fundamental roles in our solver: first, it specifies the C^1 discontinuity of ψ in the Poisson's equation discretized on the background Cartesian grid; second, it denotes the boundary of the immersed material to which the Helmholtz force is exerted.

4.1 Level Set

We use an implicit level-set function discretized on a Cartersian grid to capture the interface evolution of a magnetic material immersed in a magnetic field:

$$\varphi = \varphi(\boldsymbol{r}) = \begin{cases} +\min_{\boldsymbol{r}'\in\Sigma} |\boldsymbol{r} - \boldsymbol{r}'|, & \boldsymbol{r} \notin \Omega, \\ 0, & \boldsymbol{r} \in \Sigma, \\ -\min_{\boldsymbol{r}'\in\Sigma} |\boldsymbol{r} - \boldsymbol{r}'|, & \boldsymbol{r} \in \Omega, \end{cases} \tag{25}$$

where the zero-level set is the interface.

Next, we re-formulate the expression of the Helmholtz force applied on the interface by using the level-set function. We first introduce a *Heaviside step function*[1] taking φ as input:

$$\theta = \theta(\varphi) = \begin{cases} 0, & \varphi < 0, \\ 1/2, & \varphi = 0, \\ 1, & \varphi > 0. \end{cases} \tag{26}$$

The gradient of the Heaviside function can be expressed as

$$\begin{aligned} \nabla\theta(\varphi(\boldsymbol{r})) &= \frac{\mathrm{d}\theta(\varphi)}{\mathrm{d}\varphi}\nabla\varphi \\ &= \delta(\varphi)\hat{\boldsymbol{n}}(\boldsymbol{r}), \end{aligned} \tag{27}$$

in which $\delta(\varphi)$ is the regular Dirac delta function. The expression for χ (Equation (12d)) can be rewritten by using φ as

$$\chi(\boldsymbol{r}) = k[1 - \theta(\varphi(\boldsymbol{r}))]. \tag{28}$$

Combining Equations (7) and (28), we can express the interfacial Helmholtz force as

$$\boldsymbol{f}_{\mathrm{m}} = \frac{\mu_0}{2} kH^2 \delta(\varphi(\boldsymbol{r}))\hat{\boldsymbol{n}}, \tag{29}$$

which shows the fact that $\delta_\Sigma(\boldsymbol{r}) = \delta(\varphi(\boldsymbol{r}))$, compared to Equation (19). Derived by integrating Equation (29) (as in Appendix A.3), the rigorous formula of the interfacial Helmholtz force is written as

$$\begin{aligned} \boldsymbol{f}_{\mathrm{m}} &= \frac{\mu_0}{2} k \left[H^2 + \frac{k^2}{4k+4} (\boldsymbol{H}\cdot\hat{\boldsymbol{n}})^2 \right] \delta(\varphi(\boldsymbol{r}))\hat{\boldsymbol{n}} \\ &\approx \frac{\mu_0}{2} kH^2\delta(\varphi(\boldsymbol{r}))\hat{\boldsymbol{n}}, \end{aligned} \tag{30}$$

where $\boldsymbol{H}$ is extended to the interface by Equation (21), and the last approximation holds when k is small enough.

Smoothed step function. Numerically, we approximate the step function $\theta(\varphi)$ and its derivative $\delta(\varphi)$ using smoothed functions:

$$\tilde{\theta}(\varphi) = \begin{cases} 0, & \varphi \le -\varepsilon, \\ \frac{1}{2} + \frac{\varphi}{2\varepsilon} + \frac{1}{2\pi}\sin\frac{\pi\varphi}{\varepsilon}, & |\varphi| < \varepsilon, \\ 1, & \varphi \ge +\varepsilon, \end{cases} \tag{31}$$

$$\tilde{\delta}(\varphi) = \begin{cases} 0, & \varphi \le -\varepsilon, \\ \frac{1}{2\varepsilon} + \frac{1}{2\varepsilon}\cos\frac{\pi\varphi}{\varepsilon}, & |\varphi| < \varepsilon, \\ 0, & \varphi \ge +\varepsilon. \end{cases} \tag{32}$$

Here we assign a certain value to ε so as to extend the ideal sharp interface to a thin layer with a certain thickness. By doing this, we remove the singularity in Equation (16) and get the magnetic field continuously differentiable everywhere, but leave the definition of $\boldsymbol{H}$ in the 0-level set as shown in Equation (21).

[1] People are used to symbolizing Heaviside side function by H or θ. We choose θ in that H has already been used.

Sharp interfacial force. In spite of the smoothed χ and $\boldsymbol{H}$, leading to a continuous surface force (CSF) model, we add the Helmholtz force onto the ideal interface in a sharp fashion, which is essential to enabling a precise coupling between the magnetic tension effect and the capillary tension effect. The concentration of the continuous surface force is equivalent to the integral of Equation (29) with a certain ε, whose formula is the same as that in Appendix A.3, so the concentrated force equals to the ideally interfacial Helmholtz force (Equation (30)). Since $\boldsymbol{f}_{\mathrm{m}}$ is perpendicular to the interface everywhere, which amounts to a normal pressure, we can model the interfacial effects of $\boldsymbol{f}_{\mathrm{m}}$ in a sharp manner by rewriting Equation (30) as the Young–Laplace Equation:

$$\boldsymbol{f}_{\mathrm{m}}\,\mathrm{d}V = \Delta p\,\mathrm{d}\boldsymbol{S} = (p - p_0)\,\mathrm{d}\boldsymbol{S} \approx \frac{1}{2}k\mu_0 H^2\,\mathrm{d}\boldsymbol{S} \quad \text{in } \Sigma, \tag{33}$$

which can be further simplified as boundary conditions of p in the projection step using the ghost fluid method [Kang et al. 2000].

4.2 Poisson's Equation

We discretize Equation (16) on a Cartersian MAC grid as

$$\nabla\cdot\beta\nabla x = b, \tag{34}$$

with the unknowns stored on the cell centers and the spatially varying coefficients β stored on the faces of the grid. For each face, the value of β is approximated by Equation (31). The jump condition of β across the interface is treated using the smoothed step function introduced in Equation (31). Equation (34) is discretized using a standard finite-difference scheme and solved by a multi-grid preconditioned conjugate gradient solver [McAdams et al. 2010] on the MAC grid. Substituting β, x and b with $1+\chi$, ψ and $\nabla\cdot\chi\boldsymbol{H}_{\mathrm{ext}}$ respectively, we take an 1D case as an example. The finite difference scheme with varying coefficients for the cell i is given by:

$$\begin{aligned} &\frac{\left(1+\chi_{i+1/2}\right)(\psi_{i+1}-\psi_i) - \left(1+\chi_{i-1/2}\right)(\psi_i - \psi_{i-1})}{(\Delta x)^2} \\ &\quad = \frac{\chi_{i+1/2}(h_{i+1}-h_i) - \chi_{i-1/2}(h_i - h_{i-1})}{\Delta x} \end{aligned} \tag{35}$$

with h as the 1D component of $\boldsymbol{H}_{\mathrm{ext}}$, Δx as the cell size, the integer subscripts (i, $i-1$ and $i+1$) denote cell indices and the ones with halves denote the face indices.

4.3 Temporal Evolution

We take the temporal evolution of a ferrofluid immersed in an external magnetic field as a examplification of our numerical solver. The scheme can be generalized to other physical systems with different model implementations as demonstrated in our result section. In each timestep, the algorithm updates the states of the system using the following steps (also sketched in Figure 4):

(1) Advect the level-set φ and the velocity field $\boldsymbol{u}$ on the grid using the semi-Lagrangian method and reinitialize φ using the fast

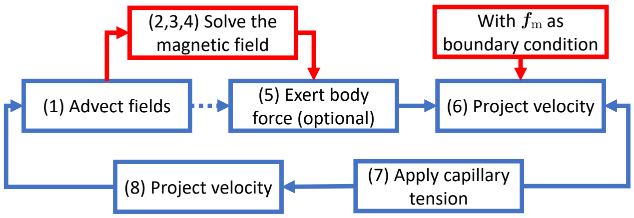

Fig. 4. The pipeline sketch of the temporal evolution of a ferrofluid. New components (painted red) are added on the basis of the standard industrial pipeline (painted blue) for fluid simulation.

marching method [Sethian 1996]:

$$\varphi \leftarrow \varphi - \Delta t(\boldsymbol{u} \cdot \nabla \varphi),$$
$$\boldsymbol{u} \leftarrow \boldsymbol{u} - \Delta t(\boldsymbol{u} \cdot \nabla \boldsymbol{u}).$$

(2) Update the magnetic susceptibility χ on the grid:

$$\chi \leftarrow k\left(1 - \tilde{\theta}\right).$$

(3) Update the potential function ψ by solving the Poisson equation (Equation (35)) in Γ discretized on the background grid using the preconditioned conjugate gradient method (PCG):

$$\begin{cases} \nabla \cdot (1+\chi)\nabla\psi = \nabla \cdot \chi \boldsymbol{H}_{\text{ext}}, & \text{in } \Gamma, \\ \nabla\psi \cdot \hat{\boldsymbol{n}}' = 0 & \text{in } \partial\Gamma, \end{cases}$$

with $\hat{\boldsymbol{n}}'$ as the normal vector of $\partial\Gamma$. This Neumann boundary condition acts as so-called *magnetic shielding*, which is used to replace the boundary condition at infinity. We should choose a reference point $\boldsymbol{r}_0$ with $\psi(\boldsymbol{r}_0) = 0$ before solving the linear system.

(4) Update the magnetic field $\boldsymbol{H}$ (Equation (17)):

$$\boldsymbol{H} = \boldsymbol{H}_{\text{ext}} - \nabla\psi.$$

(5) (Optional) Exert body forces (e.g., gravity):

$$\boldsymbol{u} \leftarrow \boldsymbol{u} + \Delta t \boldsymbol{g}.$$

(6) Apply the Helmholtz surface tension as a pressure jump and solve the Poisson's equation in Ω to enforce incompressibility. The Poisson system with the boundary conditions yields the form

$$\begin{cases} \nabla \cdot (\boldsymbol{u} - \Delta t \nabla p) = 0, & \text{in } \Omega, \\ p = p_0 + \dfrac{1}{2} k \mu_0 H^2 & \text{on the air-liquid interface,} \\ (\boldsymbol{u} - \boldsymbol{u}_{\text{solid}}) \cdot \hat{\boldsymbol{n}} = 0 & \text{on the solid-liquid interface,} \end{cases}$$

followed by $\boldsymbol{u} \leftarrow \boldsymbol{u} - \Delta t \nabla p$.

(7) Apply the capillary surface tension on the interface using a semi-implicit method [Zheng et al. 2006]. This linear system is written as

$$\frac{\boldsymbol{u}' - \boldsymbol{u}}{\Delta t} = \sigma\tilde{\delta}(\varphi)\left[\Delta t \nabla^2 \boldsymbol{u}' - \kappa\hat{\boldsymbol{n}} - \Delta t\left(\kappa \frac{\partial \boldsymbol{u}}{\partial \hat{\boldsymbol{n}}} + \frac{\partial^2 \boldsymbol{u}}{\partial \hat{\boldsymbol{n}}^2}\right)\right]$$

where $\partial/\partial\hat{\boldsymbol{n}} = \hat{\boldsymbol{n}} \cdot \nabla$ and $\partial^2/\partial^2\hat{\boldsymbol{n}} = \hat{\boldsymbol{n}} \cdot \boldsymbol{D}^2 \cdot \hat{\boldsymbol{n}}$ with $\boldsymbol{D}^2$ as the *Hessian matrix*, followed by $\boldsymbol{u} \leftarrow \boldsymbol{u}'$.

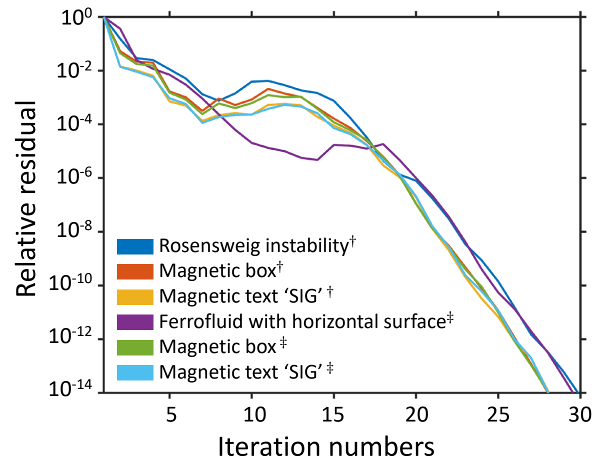

Fig. 5. Relative residuals of magnetic fields as the iteration number increases in our multi-grid solver for different configurations. † denotes the uniform external field while ‡ denotes the external field induced by a magnet.

(8) Apply another projection step to enforce the divergence-free condition for the final state. The Poisson system with the boundary conditions is written as

$$\begin{cases} \nabla \cdot (\boldsymbol{u} - \Delta t \nabla p) = c, & \text{in } \Omega, \\ p = p_0 & \text{on the air-liquid interface,} \\ (\boldsymbol{u} - \boldsymbol{u}_{\text{solid}}) \cdot \hat{\boldsymbol{n}} = 0 & \text{on the solid-liquid interface,} \end{cases}$$

with c as a volume correction term [Losasso et al. 2008], followed by $\boldsymbol{u} \leftarrow \boldsymbol{u} - \Delta t \nabla p$.

In our implementation, for a single-phase fluid, we rely on the numerical viscosity introduced by the semi-Lagrangian advection [Fedkiw et al. 2001] and ignore the viscosity term in Equation (22). As to multi-phase examples (e.g., Figure 14), the semi-implicit surface tension in Step (7) is replaced by an implicit viscosity solver [Zhu et al. 2014].

Among these steps, advection (1), body force (5), projection (6, without adding Helmholtz), surface tension or viscosity (7), and second projection (8) compose a standard industrial pipeline for fluid simulation with an implicit term (see [Bridson 2015] for details). Our magnetic ferrofluid solver modifies the pipeline by adding three additional steps (Steps (2) to (4)) and the Helmholtz boundary in (6), with only Step (3) acting as a nontrivial overhead in addition to the existing stages.

The pipeline can be modified to accommodate the magnetic deformable bodies or rigid bodies in a straightforward manner. For example, for a deformable magnetic body, Steps (6) to (8) can be replaced by a finite element elastic solver with the Helmholtz force applied on each element computed as the local pressure multiplying the area of each surface element (see Equation (33)).

By defining more level sets to track the surface of each material, it is easy to generalize this pipeline to multi-physics systems.

5 SIMULATION RESULTS

We evaluate the efficacy of our method by a set of examples for magnetic phenomena simulation, including magnetic fluid, solid, soft

Figure	Scene Description†	External Field	Resolution	Cell Size (Δx/m)	# of time steps‡	Elapsed time
5	Convergence test	Uniform / magnet	192×192	6.250×10^{-4}	1×1	0.15 s
6	Accuracy test	Uniform	$[96, 1920] \times [96, 1920]$	$[6.25, 125] \times 10^{-5}$	1×1	[0.07, 54] s
11	Rosensweig instability	Uniform	$192 \times 128 \times 192$	6.250×10^{-4}	200×14.0	23.1 h
12	Ferrofluid Taichi	Uniform	$512 \times 256 \times 512$	7.032×10^{-4}	282×12.3	28.9 d
8	Dancing ferrofluid I	Uniform	$192 \times 192 \times 192$	6.250×10^{-4}	500×22.4	6.5 d
9	Dancing ferrofluid II	Magnet	$192 \times 192 \times 192$	6.250×10^{-4}	3000×6.3	11.2 d
10	Magnetic induction lines	Uniform	$384 \times 128 \times 128$	6.250×10^{-4}	350×2.1	4.5 h
16	Magnetic rigid box	Magnet	$256 \times 192 \times 192$	6.250×10^{-4}	700×29.7	1.2 h
17	Magnetic lotus	Magnet	$192 \times 192 \times 192$	1.563×10^{-2}	750×2	21.8 h
13	Magnetic octopus	Uniform	$192 \times 128 \times 128$	1.563×10^{-1}	500×2	7.4 h
14	Two-phase flow*	Radial	192×192	6.250×10^{-4}	$200 \times [24.2, 35.5]$	[12, 18] min
15	Solid-fluid coupling	Magnet	384×384	3.125×10^{-3}	1000×13.6	2.3 h

† All these scenes use realistic physical values, including $\mu_0 = 4\pi \times 10^{-7}$ N/A^2, $k = 0.33$, $g = 9.8$ m/s^2, $\sigma = 7.28 \times 10^{-2}$ N/m, $\rho_{\text{water}} = 1.0 \times 10^3$ kg/m^3 and $\rho_{\text{iron}} = 7.8 \times 10^3$ kg/m^3 if no special instructions.
‡ The number of time steps is expressed in the product of two multipliers which are the (accurate) number of frames and the (averaged) number of time steps per frame. The latter is subject to the CFL condition.
* We set $\nu = 8.0 \times 10^{-2}$ m^2/s in this scene.

Table 2. Simulation parameters for the examples.

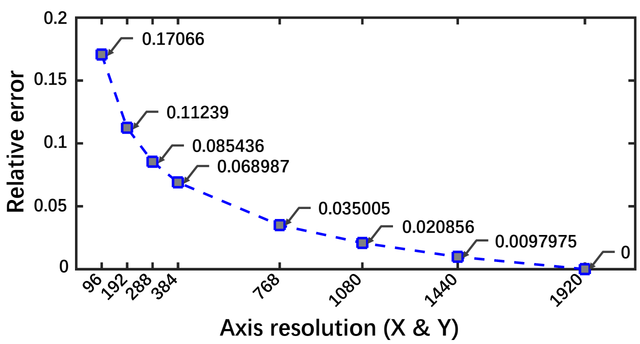

Fig. 6. Relative errors of the internal magnetic field at different resolutions, calculated with Equation (36).

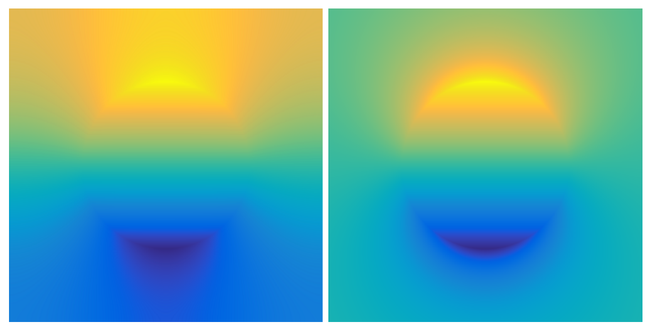

(a) Magnetic shielding; (b) Far-field condition.

Fig. 7. Comparison of magnetic fields with different boundary conditions. The left one is the heat map of linearly interpolated ψ at the resolution of 1920×1920, with magnetic shielding, and the right one is that of ψ taken from an analytical solution to the same scene, with the boundary condition at infinity.

body, and multi-phase couplings. The simulation parameter settings are summarized in Table 2. These experiments were performed on a 6-core 3.2GHz Intel(R) Core(TM) i7-8700 desktop with 16 GB RAM.

Convergence of the magnetic field. First of all, we evaluate the convergence of our multi-grid solver for magnetic fields. We put various magnetic objects inside different external fields, and then solve the internal field at the resolution of 192×192. Figure 5 illustrates convergence curves of different configurations, where we can see that such a numerical solver is universally stable and efficient.

Accuracy of the magnetic field. As to the accuracy of the magnetic field, we put a magnetic sphere inside a uniform external field, and then solve the internal magnetic field at different resolutions. For the purpose of quantitative analysis, we sample more than 10^5 points $(\boldsymbol{r}_1, \boldsymbol{r}_2, \boldsymbol{r}_3, \ldots, \boldsymbol{r}_n)$ uniformly distributed in the domain and measure the relative errors based on the following equation:

$$\text{Relative error} = \frac{\sqrt{\frac{1}{3n}\sum_{i=1}^{n}(\nabla\psi(\boldsymbol{r}_i) - \nabla\psi'(\boldsymbol{r}_i))^2}}{\sqrt{\frac{1}{3n}\sum_{i=1}^{n}\nabla\psi'^2(\boldsymbol{r}_i)}}, \tag{36}$$

where $3n$ equals to the number of degrees of freedom. Here ψ' is taken at the highest resolution (1920×1920), and ψ is taken at a lower one. Both of them are linearly interpolated. Figure 6 shows the line chart of relative errors with respect to different resolutions. This experiment suggests that even at a medium resolution, the magnetic field can be fairly accurate. As shown in Figure 7, we draw the heat map of linearly interpolated ψ at the resolution of 1920×1920 and that of ψ from an analytical solution with the boundary condition at infinity side by side. We can see that the field with magnetic shielding is significantly different from that with the far-field condition near the boundary, but achieves a comparable accuracy around the interface.

Rosensweig instability. We first simulate the ferrofluid phenomena of Rosensweig instability [Rosensweig 1985] as shown in Figure 11. When a paramagnetic fluid is subjected to a strong vertical magnetic

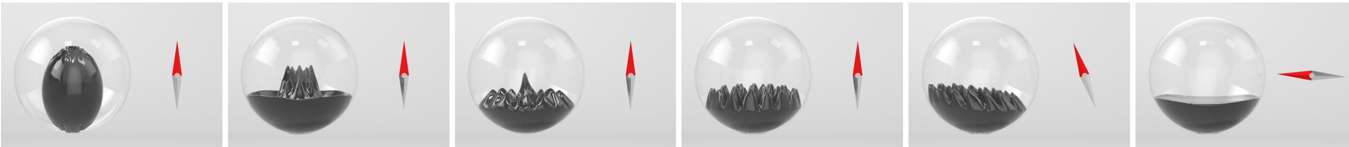

Fig. 8. Ferrofluid droplet falls inside the crystal ball and is magnetized by a rotating external magnetic field whose direction is denoted by the compass.

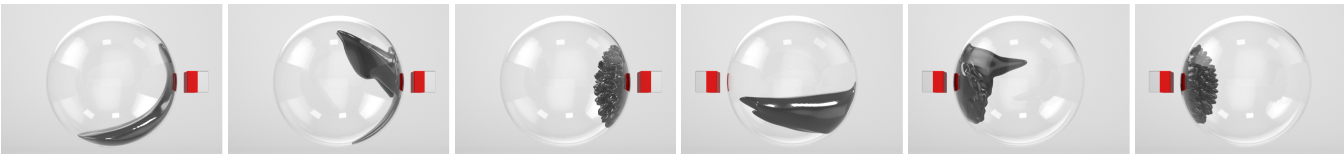

Fig. 9. Ferrofluid inside the crystal is atrracted by a moving magnet and shaping into spikes.

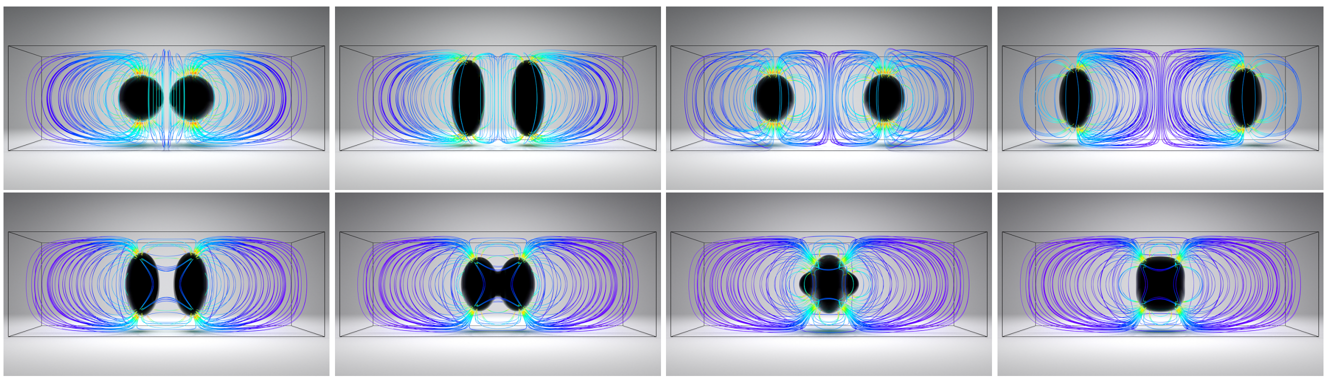

Fig. 10. Top: a uniform external field magnetizes the ferrofluid droplets and makes them separate from each other; below: the same experiment with two external fields with different signs on the left and right sides, in which case the droplets are magnetized and attracted by each other. The magnetic induction lines are visualized.

field, the surface exhibits a regular pattern of peaks and valleys. We initialize the ferrofluid in a squared container exposed to a uniformly vertical external magnetic field. When the external magnetic field is turned on, the spike structure emerges immediately and stabilizes to a steady state.

Dancing ferrofluid. As in Figure 8, we demonstrate the effects of a temporally varying external magnetic field on immersed ferrofluid within a spherical container. Influenced by gravity and the uniformly vertical external magnetic field, the droplet falls and exhibits spiky structures. Then, the external magnetic field begins to rotate globally, guiding the deformation of the spikes on the fluid surface. We use the compass to illustrate the direction of the external magnetic field. As in Figure 9, we demonstrate the effects of an external magnetic field that varies both spatially and temporally, as the magnet exhibits both rotational and translational motion. The ferrofluid in the spherical container reacts to the magnet at high speed by exhibiting vivid motions and geometries.

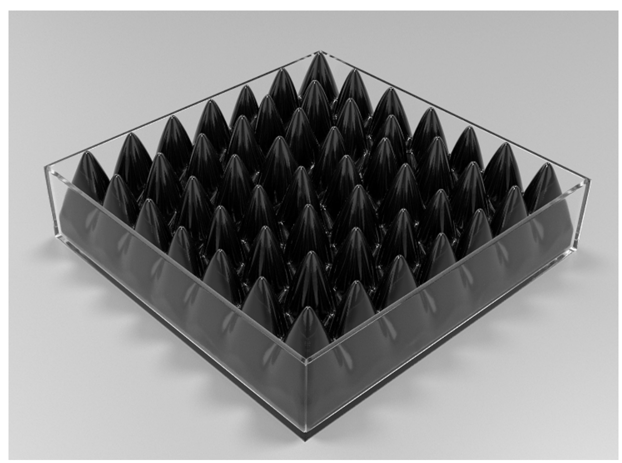

Fig. 11. Rosensweig instability of ferrofluid under uniform external magnetic field.

Magnetic induction lines. Two magnets with the same polarization will separate from each other, while two magnets with contrary polarization will approach to each other. As in Figure 10, we illustrate this scientific fact by simulating the interaction between two

Fig. 12. Ferrofluid Taichi simulation.

(a) $k = 0.16$; (b) $k = 0.33$; (c) $k = 0.50$.

Fig. 14. Two-phase magnetic liquid: the orange part is ferrofluid with susceptibilty k while the black part is normal water, after 0.4 second.

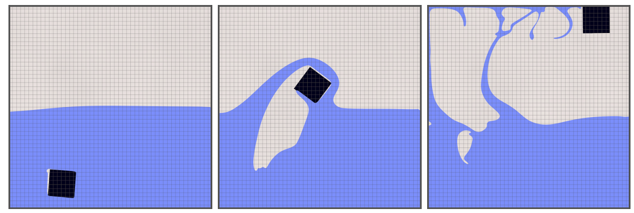

Fig. 15. Coupling in 2D: an iron box under water is attracted by a magnet on the top right.

weightless ferrofluid droplets and visualizing the induced magnetic lines within the entire space. It is the two types of internal magnetic fields that determine the difference of droplet behaviors.

Ferrofluid Taichi. As shown in Figure 12, we simulate the evolution of ferrofluid inside a container with a Taichi shape, at the resolution of $512 \times 512 \times 256$ in slow motion. Such an example highlights the scalability of our numerical method.

Magnetic rigid box. As in Figure 16, we simulate a magnetic rigid body interacting with a magnet to showcase the capability of our solver in simulating interaction between magnetic rigid bodies. We present two numerical experiments, one with an internal magnetic field and one without. From these, we can learn that if we just consider the one-way effect from the external field to the magnetic objects, the results will be distorted to some extent.

Magnetic lotus. As shown in Figure 17, we illustrate the beauty of the interaction between a soft magnetic structure and a translating magnet. The lotus petals are modeled as thin elastic sheets that are magnetized within the external magnetic field and exhibit visually vivid deformations when interacting with the kinematic magnet source. In inset plots of this figure, the deformations are demonstrated by the von Mises strain distribution.

Magnetic octopus. We put a magnetic octopus inside a uniform external magnetic field, as shown in Figure 13. All the tentacles have the same polarization, so they tend to repulse each other, making the body open up.

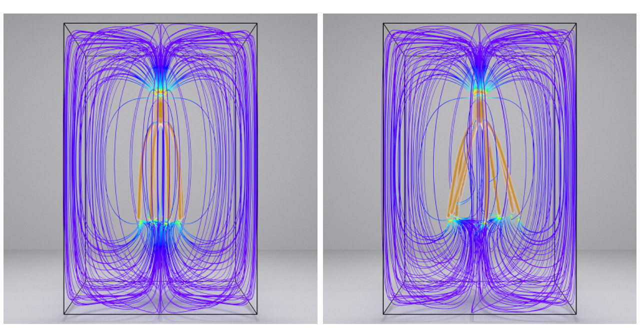

Fig. 13. Simulation of a magnetic octopus, with the internal field visualized.

Two-phase flow. To test our scheme in a multi-physics system, first we set a scene of two-phase flow. As in Figure 14, the brown part is the ferrofluid, while the black one is the normal water. When a radial external field is applied, the interface will be deformed, shaped into gorgeous patterns, where deformation becomes larger as k increases. Such a setting is inspired by [Anjos et al. 2019].

Solid-fluid coupling. Another multi-physics system is a coupling between a magnetic rigid body and normal water, shown in Figure 15. At first, a magnetic box is sunken to the bottom of our simulation water tank. Because a magnet is located on the top right, the box is attracted and flies out of the water, which generates huge splashes.

6 DISCUSSIONS AND CONCLUSIONS

We have presented a novel approach to modeling the interactions between magnetic fields and various forms of magnetizable systems in a unified way, which enables efficient and effective simulation of a broad spectrum of magnetic phenomena, including magnetic fluids, soft bodies, rigid bodies, and their interactions. At the heart of our approach lies a two-way coupling mechanism between the background Eulerian magnetic field and the immersed Eulerian (or Lagrangian) mechanical system, enabled by an interfacial Helmholtz force. We devise a numerical scheme, motivated by the immersed boundary method, to effectively treat the coupling by solving only one additional Poisson equation with boundary jump conditions. Our approach shares inherent common threads with an array of numerical methods that are widely used in VFX commercial software, e.g., level-set liquid, grid-based Poisson solver, immersed boundary method, advection-projection scheme, etc., enabling an immediate and seamless integration of our approach into an industrial pipeline, to create a broad range of novel magnetic phenomena simulations.

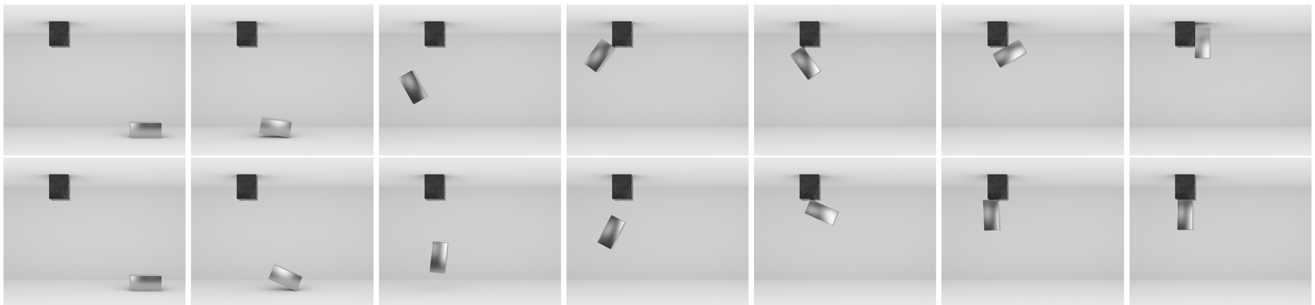

Fig. 16. Top: iron box attracted by a magnet, without magnetization; below: iron box attracted by a magnet, with magnetization.

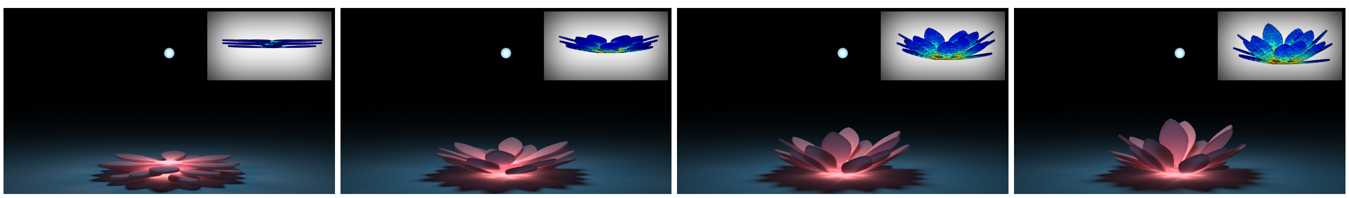

Fig. 17. A soft magnetic lotus attracted by a moving magnet, with deformations demonstrated by the von Mises strain distribution in the upper-right corner.

Our current implementation suffers from two main limitations. First, the way to add Helmholtz force is explicit, which might cause numerical instability potentially and therefore limits the system's CFL condition. To be specific, we test the CFL number, denoted α, for a two-dimensional experiment of Rosensweig instability, as shown in Figure 18. The ferrofluid begins to vibrate as a whole near the equilibrium position when α exceeds 2. If $\alpha > 4$, local vibrations on the surface also appear. This will lead to mass ejection when $\alpha > 7$. Second, the immersed boundary coupling between the magnetic field and the mechanical system is essentially a weakly coupling scheme. It could suffer from numerical issues when simulating a strongly coupled system in which a monolithic scheme [Robinson-Mosher et al. 2011] exhibits inherent strength.

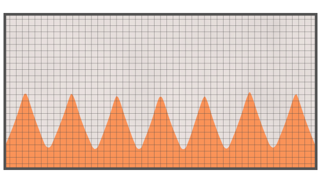

(a) $\alpha = 1.0$ (equilibrium);

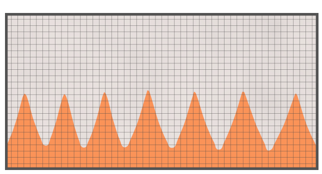

(b) $\alpha = 3.0$ (whole vibration);

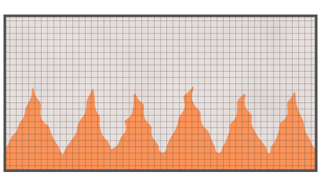

(c) $\alpha = 5.0$ (local vibration);

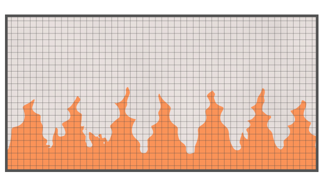

(d) $\alpha = 8.0$ (mass ejection).

Fig. 18. Ferrofluid behaviors in the experiment of 2D Rosensweig instability at the resolution of 192×96, taking different representative CFL numbers.

One interesting direction for future work is to devise a boundary element method [James and Pai 1999] to model the interfacial magnetic-mechanical interactions. It will be interesting to see our interfacial Helmholtz solver incorporated into a surface-only liquid solver (e.g., [Da et al. 2016b]) for computational benefits in that volumetric discretization is completely done away. As an immediate next step, another direction lies in the linearization of the Helmholtz jump which can potentially lead to a fully implicit surface tension solver by integrating both Helmholtz and capillary effects in a unified way, which, on the other hand, can potentially boost the numerical performance as well. While we have merely touched upon the simulation of multi-phase ferrofluid, which already exhibits astonishing appearance and complexity, there are still a broad array of interesting avenues in magnetic substance simulation with inherently complex interfacial physics to explore. Thanks to the Eulerian nature of our approach, we are able to visualize the simulation results in a scientific manner, which might prove helpful to the collaboration between physicists and fluid mechanics scientists for their better understanding of these intricate magnetic phenomena by providing them an effective numerical tool to conduct a broad variety of parameter studies and numerical analysis.

ACKNOWLEDGMENTS

We thank the anonymous reviewers for their constructive comments. This work was supported in part by National Key R&D Program of China (2019YFF0302902, 2018YFB1403900). Bo Zhu acknowledges the funding supports from Neukom Institute CompX Faculty Grant, Burke Research Initiation Award, Toyota TEMA North America Inc, ByteDance Inc, and NSF 1919647. We would like to thank Yongning Zhu from Tongji University, Haowei Han and Lingbo Qin from Light Chaser Animation Studios for their help on level-set data

exportation and video generations. The Houdini Education license is credited for the video generations.

REFERENCES

Mridul Aanjaneya, Ming Gao, Haixiang Liu, Christopher Batty, and Eftychios Sifakis. 2017. Power Diagrams and Sparse Paged Grids for High Resolution Adaptive Liquids. *ACM Trans. Graph.* 36, 4, Article 140 (July 2017), 12 pages.

Ryoichi Ando and Reiji Tsuruno. 2011. A Particle-Based Method for Preserving Fluid Sheets. In *Proceedings of the 2011 ACM SIGGRAPH/Eurographics Symposium on Computer Animation (SCA '11)*. Association for Computing Machinery, New York, NY, USA, 7–16.

Pedro H. A. Anjos, Gabriel D. Carvalho, Sérgio A. Lira, and José A. Miranda. 2019. Wrinkling and folding patterns in a confined ferrofluid droplet with an elastic interface. *Physical Review E* 99, 2 (2019), 022608.

Christopher Batty and Robert Bridson. 2008. Accurate Viscous Free Surfaces for Buckling, Coiling, and Rotating Liquids. In *Proceedings of the 2008 ACM SIGGRAPH/Eurographics Symposium on Computer Animation (SCA '08)*. Eurographics Association, Goslar, DEU, 219–228.

Christopher Batty, Andres Uribe, Basile Audoly, and Eitan Grinspun. 2012. Discrete Viscous Sheets. *ACM Transactions on Graphics (Proceedings of SIGGRAPH 2012)* 31, 4 (2012), 113:1–113:7.

Miklós Bergou, Basile Audoly, Etienne Vouga, Max Wardetzky, and Eitan Grinspun. 2010. Discrete Viscous Threads. *ACM Trans. Graph.* 29, 4, Article 116 (July 2010), 10 pages.

Robert Bridson. 2015. *Fluid simulation for computer graphics* (2nd ed.). AK Peters/CRC Press, Boca Raton, FL, USA.

Tyson Brochu, Todd Keeler, and Robert Bridson. 2012. Linear-Time Smoke Animation with Vortex Sheet Meshes. In *Proceedings of the ACM SIGGRAPH/Eurographics Symposium on Computer Animation (SCA '12)*. Eurographics Association, Goslar, DEU, 87–95.

Yuan Cao and Z.J. Ding. 2014. Formation of hexagonal pattern of ferrofluid in magnetic field. *Journal of Magnetism and Magnetic Materials* 355 (2014), 93–99.

Fang Da, Christopher Batty, and Eitan Grinspun. 2014. Multimaterial Mesh-Based Surface Tracking. *ACM Trans. Graph.* 33, 4, Article 112 (July 2014), 11 pages.

Fang Da, Christopher Batty, Chris Wojtan, and Eitan Grinspun. 2015. Double Bubbles sans Toil and Trouble: Discrete Circulation-Preserving Vortex Sheets for Soap Films and Foams. *ACM Trans. Graph.* 34, 4, Article 149 (July 2015), 9 pages.

Fang Da, David Hahn, Christopher Batty, Chris Wojtan, and Eitan Grinspun. 2016a. Surface-Only Liquids. *ACM Trans. Graph.* 35, 4, Article 78 (July 2016), 12 pages.

Fang Da, David Hahn, Christopher Batty, Chris Wojtan, and Eitan Grinspun. 2016b. Surface-Only Liquids. *ACM Trans. Graph.* 35, 4, Article 78 (July 2016), 12 pages.

Albert Einstein and Jakob Laub. 1908. Über die im elektromagnetischen Felde auf ruhende Körper ausgeübten ponderomotorischen Kräfte. *Annalen der Physik* 331, 8 (1908), 541–550.

Yu Fang, Minchen Li, Ming Gao, and Chenfanfu Jiang. 2019. Silly Rubber: An Implicit Material Point Method for Simulating Non-Equilibrated Viscoelastic and Elastoplastic Solids. *ACM Trans. Graph.* 38, 4, Article 118 (July 2019), 13 pages.

Ronald Fedkiw, Jos Stam, and Henrik Wann Jensen. 2001. Visual Simulation of Smoke. In *Proceedings of the 28th Annual Conference on Computer Graphics and Interactive Techniques (SIGGRAPH '01)*. Association for Computing Machinery, New York, NY, USA, 15–22.

Yun (Raymond) Fei, Christopher Batty, Eitan Grinspun, and Changxi Zheng. 2018. A Multi-Scale Model for Simulating Liquid-Fabric Interactions. *ACM Trans. Graph.* 37, 4, Article 51 (July 2018), 16 pages.

Yun (Raymond) Fei, Christopher Batty, Eitan Grinspun, and Changxi Zheng. 2019. A Multi-Scale Model for Coupling Strands with Shear-Dependent Liquid. *ACM Trans. Graph.* 38, 6, Article 190 (Nov. 2019), 20 pages.

Yun (Raymond) Fei, Henrique Teles Maia, Christopher Batty, Changxi Zheng, and Eitan Grinspun. 2017. A Multi-Scale Model for Simulating Liquid-Hair Interactions. *ACM Trans. Graph.* 36, 4, Article 56 (July 2017), 17 pages.

Nick Foster and Ronald Fedkiw. 2001. Practical Animation of Liquids. In *Proceedings of the 28th Annual Conference on Computer Graphics and Interactive Techniques (SIGGRAPH '01)*. Association for Computing Machinery, New York, NY, USA, 23–30.

Ming Gao, Andre Pradhana Tampubolon, Chenfanfu Jiang, and Eftychios Sifakis. 2017. An Adaptive Generalized Interpolation Material Point Method for Simulating Elastoplastic Materials. *ACM Trans. Graph.* 36, 6, Article 223 (Nov. 2017), 12 pages.

Ali Ghaffari, Seyed Hassan Hashemabadi, and Mansour Bazmi. 2015. CFD simulation of equilibrium shape and coalescence of ferrofluid droplets subjected to uniform magnetic field. *Colloids and Surfaces A: Physicochemical and Engineering Aspects* 481 (2015), 186–198.

Christian Gollwitzer, Gunar Matthies, Reinhard Richter, Ingo Rehberg, and Lutz Tobiska. 2007. The surface topography of a magnetic fluid: a quantitative comparison between experiment and numerical simulation. *Journal of fluid mechanics* 571 (2007), 455–474.

Francis H. Harlow and J. Eddie Welch. 1965. Numerical calculation of time-dependent viscous incompressible flow of fluid with free surface. *The Physics of Fluids* 8, 12 (1965), 2182–2189.

Xiaowei He, Ning Liu, Guoping Wang, Fengjun Zhang, Sheng Li, Songdong Shao, and Hongan Wang. 2012. Staggered Meshless Solid-Fluid Coupling. *ACM Trans. Graph.* 31, 6, Article 149 (Nov. 2012), 12 pages.

Jeong-Mo Hong, Tamar Shinar, and Ronald Fedkiw. 2007. Wrinkled Flames and Cellular Patterns. *ACM Trans. Graph.* 26, 3 (July 2007), 47–es.

Libo Huang, Torsten Hädrich, and Dominik L. Michels. 2019. On the Accurate Large-scale Simulation of Ferrofluids. *ACM Trans. Graph.* 38, 4, Article 93 (July 2019), 15 pages.

Tomokazu Ishikawa, Yonghao Yue, Kei Iwasaki, Yoshinori Dobashi, and Tomoyuki Nishita. 2013. Visual Simulation of Magnetic Fluid Using a Procedural Approach for Spikes Shape. In *Computer Vision, Imaging and Computer Graphics. Theory and Application*. Springer Berlin Heidelberg, Berlin, Heidelberg, 112–126.

Doug L. James and Dinesh K. Pai. 1999. ArtDefo: Accurate Real Time Deformable Objects. In *Proceedings of the 26th Annual Conference on Computer Graphics and Interactive Techniques (SIGGRAPH '99)*. ACM Press/Addison-Wesley Publishing Co., USA, 65–72.

Stefan Jeschke, Tomáš Skřivan, Matthias Müller-Fischer, Nuttapong Chentanez, Miles Macklin, and Chris Wojtan. 2018. Water Surface Wavelets. *ACM Trans. Graph.* 37, 4, Article 94 (July 2018), 13 pages.

Stefan Jeschke and Chris Wojtan. 2015a. Water Wave Animation via Wavefront Parameter Interpolation. *ACM Trans. Graph.* 34, 3, Article 27 (May 2015), 14 pages.

Stefan Jeschke and Chris Wojtan. 2015b. Water Wave Animation via Wavefront Parameter Interpolation. *ACM Trans. Graph.* 34, 3, Article 27 (May 2015), 14 pages.

Stefan Jeschke and Chris Wojtan. 2017. Water Wave Packets. *ACM Trans. Graph.* 36, 4, Article 103 (July 2017), 12 pages.

Chenfanfu Jiang, Theodore Gast, and Joseph Teran. 2017. Anisotropic Elastoplasticity for Cloth, Knit and Hair Frictional Contact. *ACM Trans. Graph.* 36, 4, Article 152 (July 2017), 14 pages.

Yupeng Jiang, Minchen Li, Chenfanfu Jiang, and Fernando Alonso-marroquin. 2019. A hybrid material-point spheropolygon-element method for solid and granular material interaction. arXiv:cs.CE/1909.13655

Myungjoo Kang, Ronald P. Fedkiw, and Xu-Dong Liu. 2000. A boundary condition capturing method for multiphase incompressible flow. *Journal of Scientific Computing* 15, 3 (2000), 323–360.

Seung-Wook Kim, Sun Young Park, and Junghyun Han. 2018. Magnetization Dynamics for Magnetic Object Interactions. *ACM Trans. Graph.* 37, 4, Article 121 (July 2018), 13 pages.

Theodore Kim, Jerry Tessendorf, and Nils Thürey. 2013. Closest Point Turbulence for Liquid Surfaces. *ACM Trans. Graph.* 32, 2, Article 15 (April 2013), 13 pages.

Gergely Klár, Theodore Gast, Andre Pradhana, Chuyuan Fu, Craig Schroeder, Chenfanfu Jiang, and Joseph Teran. 2016. Drucker-Prager Elastoplasticity for Sand Animation. *ACM Trans. Graph.* 35, 4, Article 103 (July 2016), 12 pages.

Egor Larionov, Christopher Batty, and Robert Bridson. 2017. Variational Stokes: A Unified Pressure-Viscosity Solver for Accurate Viscous Liquids. *ACM Trans. Graph.* 36, 4, Article 101 (July 2017), 11 pages.

Haixiang Liu, Yuanming Hu, Bo Zhu, Wojciech Matusik, and Eftychios Sifakis. 2018. Narrow-Band Topology Optimization on a Sparsely Populated Grid. *ACM Trans. Graph.* 37, 6, Article 251 (Dec. 2018), 14 pages.

Haixiang Liu, Nathan Mitchell, Mridul Aanjaneya, and Eftychios Sifakis. 2016. A Scalable Schur-Complement Fluids Solver for Heterogeneous Compute Platforms. *ACM Trans. Graph.* 35, 6, Article 201 (Nov. 2016), 12 pages.

Jing Liu, Yit Fatt Yap, and Nam-Trung Nguyen. 2011. Numerical study of the formation process of ferrofluid droplets. *Physics of Fluids* 23, 7 (2011), 072008.

Frank Losasso, Ronald Fedkiw, and Stanley Osher. 2006a. Spatially adaptive techniques for level set methods and incompressible flow. *Computers & Fluids* 35, 10 (2006), 995–1010.

Frank Losasso, Frédéric Gibou, and Ron Fedkiw. 2004. Simulating Water and Smoke with an Octree Data Structure. *ACM Trans. Graph.* 23, 3 (Aug. 2004), 457–462.

Frank Losasso, Geoffrey Irving, Eran Guendelman, and Ronald Fedkiw. 2006b. Melting and burning solids into liquids and gases. *IEEE Transactions on Visualization and Computer Graphics* 12, 3 (2006), 343–352.

Frank Losasso, Jerry Talton, Nipun Kwatra, and Ronald Fedkiw. 2008. Two-way coupled SPH and particle level set fluid simulation. *IEEE Transactions on Visualization and Computer Graphics* 14, 4 (2008), 797–804.

James Clerk Maxwell. 1865. A dynamical theory of the electromagnetic field. *Philosophical Transactions of the Royal Society of London* 155 (1865), 459–512.

A. McAdams, E. Sifakis, and J. Teran. 2010. A Parallel Multigrid Poisson Solver for Fluids Simulation on Large Grids. In *Proceedings of the 2010 ACM SIGGRAPH/Eurographics Symposium on Computer Animation (SCA '10)*. Eurographics Association, Goslar, DEU, 65–74.

Hermann Minkowski. 1908. Die Grundgleichungen für die elektromagnetischen Vorgänge in bewegten Körpern. *Nachrichten von der Gesellschaft der Wissenschaften zu Göttingen, Mathematisch-Physikalische Klasse* 1908, 1 (1908), 53–111.

Duc Nguyen, Doug Enright, and Ron Fedkiw. 2003. Simulation and animation of fire and other natural phenomena in the visual effects industry. Western States Section, Combustion Institute, Fall Meeting, UCLA.

Duc Quang Nguyen, Ronald Fedkiw, and Henrik Wann Jensen. 2002. Physically Based Modeling and Animation of Fire. *ACM Trans. Graph.* 21, 3 (July 2002), 721–728.

James F. O'brien and Jessica K. Hodgins. 1995. Dynamic simulation of splashing fluids. In *Proceedings Computer Animation '95*. IEEE, Geneva, Switzerland, Switzerland, 198–205.

Curtis M. Oldenburg, Sharon E. Borglin, and George J. Moridis. 2000. Numerical simulation of ferrofluid flow for subsurface environmental engineering applications. *Transport in Porous Media* 38, 3 (2000), 319–344.

Stanley Osher and Ronald P Fedkiw. 2005. *Level set methods and dynamic implicit surfaces*. Springer, New York, NY, USA.

Charles Peskin. 1972. Flow patterns around heart valves: A numerical method. *J. Comput. Phys.* 10, 2 (1972), 252–271.

Daniel Ram, Theodore Gast, Chenfanfu Jiang, Craig Schroeder, Alexey Stomakhin, Joseph Teran, and Pirouz Kavehpour. 2015. A Material Point Method for Viscoelastic Fluids, Foams and Sponges. In *Proceedings of the 14th ACM SIGGRAPH / Eurographics Symposium on Computer Animation (SCA '15)*. Association for Computing Machinery, New York, NY, USA, 157–163.

Avi Robinson-Mosher, Craig Schroeder, and Ronald Fedkiw. 2011. A symmetric positive definite formulation for monolithic fluid structure interaction. *J. Comput. Phys.* 230, 4 (2011), 1547–1566.

Ronald E. Rosensweig. 1985. *Ferrohydrodynamics*. Cambridge University Press, Cambridgeshire, England, UK.

Robert Saye. 2016. Interfacial gauge methods for incompressible fluid dynamics. *Science advances* 2, 6 (2016), e1501869.

Robert I Saye and James A Sethian. 2013. Multiscale modeling of membrane rearrangement, drainage, and rupture in evolving foams. *Science* 340, 6133 (2013), 720–724.

Camille Schreck, Christian Hafner, and Chris Wojtan. 2019. Fundamental Solutions for Water Wave Animation. *ACM Trans. Graph.* 38, 4, Article 130 (July 2019), 14 pages.

Rajsekhar Setaluri, Mridul Aanjaneya, Sean Bauer, and Eftychios Sifakis. 2014. SPGrid: A Sparse Paged Grid Structure Applied to Adaptive Smoke Simulation. *ACM Trans. Graph.* 33, 6, Article 205 (Nov. 2014), 12 pages.

James A. Sethian. 1996. A fast marching level set method for monotonically advancing fronts. *Proceedings of the National Academy of Sciences* 93, 4 (1996), 1591–1595.

Dongxiao Shi, Qincheng Bi, and Rongqi Zhou. 2014. Numerical simulation of a falling ferrofluid droplet in a uniform magnetic field by the VOSET method. *Numerical Heat Transfer, Part A: Applications* 66, 2 (2014), 144–164.

Barbara Solenthaler and Markus Gross. 2011. Two-Scale Particle Simulation. *ACM Trans. Graph.* 30, 4, Article 81 (July 2011), 8 pages.

Bernhard Thomaszewski, Andreas Gumann, Simon Pabst, and Wolfgang Straßer. 2008. Magnets in Motion. *ACM Trans. Graph.* 27, 5, Article 162 (Dec. 2008), 9 pages.

Nils Thürey, Chris Wojtan, Markus Gross, and Greg Turk. 2010. A Multiscale Approach to Mesh-Based Surface Tension Flows. *ACM Trans. Graph.* 29, 4, Article 48 (July 2010), 10 pages.

Sheng Yang, Xiaowei He, Huamin Wang, Sheng Li, Guoping Wang, Enhua Wu, and Kun Zhou. 2016. Enriching SPH Simulation by Approximate Capillary Waves. In *Proceedings of the ACM SIGGRAPH/Eurographics Symposium on Computer Animation (SCA '16)*. Eurographics Association, Goslar, DEU, 29–36.

G. Yoshikawa, K. Hirata, F. Miyasaka, and Y. Okaue. 2011. Numerical Analysis of Transitional Behavior of Ferrofluid Employing MPS Method and FEM. *IEEE Transactions on Magnetics* 47, 5 (May 2011), 1370–1373.

Yonghao Yue, Breannan Smith, Christopher Batty, Changxi Zheng, and Eitan Grinspun. 2015. Continuum Foam: A Material Point Method for Shear-Dependent Flows. *ACM Trans. Graph.* 34, 5, Article 160 (Nov. 2015), 20 pages.

Yonghao Yue, Breannan Smith, Peter Yichen Chen, Maytee Chantharayukhonthorn, Ken Kamrin, and Eitan Grinspun. 2018. Hybrid Grains: Adaptive Coupling of Discrete and Continuum Simulations of Granular Media. *ACM Trans. Graph.* 37, 6, Article 283 (Dec. 2018), 19 pages.

Ruike Zhao, Yoonho Kim, Shawn A Chester, Pradeep Sharma, and Xuanhe Zhao. 2019. Mechanics of hard-magnetic soft materials. *Journal of the Mechanics and Physics of Solids* 124 (2019), 244–263.

Wen Zheng, Jun-Hai Yong, and Jean-Claude Paul. 2006. Simulation of Bubbles. In *Proceedings of the 2006 ACM SIGGRAPH/Eurographics Symposium on Computer Animation (SCA '06)*. Eurographics Association, Goslar, DEU, 325–333.

Wen Zheng, Bo Zhu, Byungmoon Kim, and Ronald Fedkiw. 2015. A new incompressibility discretization for a hybrid particle MAC grid representation with surface tension. *J. Comput. Phys.* 280 (2015), 96–142.

Bo Zhu, Minjae Lee, Ed Quigley, and Ronald Fedkiw. 2015. Codimensional Non-Newtonian Fluids. *ACM Trans. Graph.* 34, 4, Article 115 (July 2015), 9 pages.

Bo Zhu, Ed Quigley, Matthew Cong, Justin Solomon, and Ronald Fedkiw. 2014. Codimensional Surface Tension Flow on Simplicial Complexes. *ACM Trans. Graph.* 33, 4, Article 111 (July 2014), 11 pages.

Yongning Zhu and Robert Bridson. 2005. Animating Sand as a Fluid. *ACM Trans. Graph.* 24, 3 (July 2005), 965–972.

A PHYSICAL ANALYSIS

A.1 Explanation and Derivation of Magnetic Interaction

From a micro perspective, all the macro physical quantities are averaged over micro ones within a given space-time region, among which the averaged stress-energy tensor is often divided into the field term and the medium term. In classical electrodynamics, the Maxwell stress tensor $\boldsymbol{T}_\mathrm{m}$ is used to represent the interaction between electromagnetic forces and mechanical momentum, i.e., it reflects the relation between the electromagnetic field term and the medium term. Therefore, the form of the Maxwell stress tensor depends on different divisions of the averaged stress-energy tensor. In vacuum, there is no medium term, so the Maxwell stress tensor as in Equation (1) is uncontroversial, but in matter there are several opinions on the division, which results in different forms of this tensor. Besides Einstein, Laub and Minkowski, other physicists including Abraham also proposed their forms.

The magnetic force density can be computed by $\boldsymbol{f}_\mathrm{m} = \nabla \cdot \boldsymbol{T}_\mathrm{m}$. We will discuss the Kelvin force and the Helmholtz force respectively.

For the Kelvin force,

$$\begin{aligned}
\boldsymbol{f}_\mathrm{m}^\mathrm{E} &= \nabla \cdot (\boldsymbol{B} \otimes \boldsymbol{H}) - \frac{\mu_0}{2} \nabla \cdot H^2 \boldsymbol{I} \\
&= \boldsymbol{H}(\nabla \cdot \boldsymbol{B}) + \boldsymbol{B} \cdot \nabla \boldsymbol{H} - \frac{\mu_0}{2} \nabla \cdot (\boldsymbol{H} \cdot \boldsymbol{H}) \boldsymbol{I} \\
&= 0 + \boldsymbol{B} \cdot \nabla \boldsymbol{H} - \mu_0 \boldsymbol{H} \cdot \nabla \boldsymbol{H} \\
&= (\boldsymbol{B} - \mu_0 \boldsymbol{H}) \cdot \nabla \boldsymbol{H} \\
&= \mu_0 \boldsymbol{M} \cdot \nabla \boldsymbol{H},
\end{aligned} \tag{37}$$

exploiting Equation (12b), in which the term with $\nabla \cdot \boldsymbol{B}$ is eliminated confidently according to Equation (11a). Similarly, for the Helmholtz force,

$$\begin{aligned}
\boldsymbol{f}_\mathrm{m}^\mathrm{M} &= \nabla \cdot \boldsymbol{B}\boldsymbol{H} - \frac{1}{2} \nabla \cdot (\boldsymbol{B} \cdot \boldsymbol{H}) \boldsymbol{I} \\
&= \boldsymbol{H}(\nabla \cdot \boldsymbol{B}) + \boldsymbol{B} \cdot \nabla \boldsymbol{H} - \frac{1}{2} \nabla \cdot (\boldsymbol{B} \cdot \boldsymbol{H}) \boldsymbol{I} \\
&= \boldsymbol{B} \cdot \nabla \boldsymbol{H} - \frac{1}{2} \nabla \cdot (\boldsymbol{B} \cdot \boldsymbol{H}) \boldsymbol{I}.
\end{aligned} \tag{38}$$

When the linear, isotropic assumption is adopted, i.e., $\boldsymbol{M} = \chi \boldsymbol{H}$ is satisfied, the two forces are simplified as

$$\begin{aligned}
\boldsymbol{f}_\mathrm{m}^\mathrm{E} &= \mu_0 \chi \boldsymbol{H} \cdot \nabla \boldsymbol{H} \\
&= \frac{\mu_0}{2} \chi \nabla (\boldsymbol{H} \cdot \boldsymbol{H}) \\
&= \frac{\mu_0}{2} \chi \nabla \left(H^2 \right)
\end{aligned} \tag{39}$$

and

$$\begin{aligned}
\boldsymbol{f}_\mathrm{m}^\mathrm{M} &= \mu \boldsymbol{H} \cdot \nabla \boldsymbol{H} - \frac{1}{2} \nabla \cdot \mu H^2 \boldsymbol{I} \\
&= \frac{\mu_0}{2} (1 + \chi) \nabla \left(H^2 \right) - \frac{\mu_0}{2} \nabla (1 + \chi) H^2 \\
&= -\frac{\mu_0}{2} H^2 \nabla \chi.
\end{aligned} \tag{40}$$

A.2 Mechanism of Magnetization and Induction

Every atom can be considered as a dipole with an invariant magnetic moment $\boldsymbol{m}_i$ indicating its magnetic performance. If there is no external magnetic field, the orientation of atoms is totally random.

The sum of the induced magnetic fields by all these atoms is zero everywhere. That is why most substances are not magnetic on a macroscopic level. Most atoms do not react to external magnetic fields. However, some ferromagnetic atoms, including iron, cobalt and nickle, are strongly attracted by external magnetic fields and can be polarized to align with the direction of the magnetic field. This process is called *magnetization*. There are different categories of magnetism, with ferromagnetism underpinning most of the magnetic phenomena in our daily life.

In physics, the macroscopic magnetic performance is described by the vector field $\boldsymbol{M}$:

$$\boldsymbol{M} = \boldsymbol{M}(\boldsymbol{r}) = \lim_{\Delta V \to 0} \frac{\sum_i \boldsymbol{m}_i}{\Delta V}, \tag{41}$$

which summarizes all of the atoms within an infinitesimal ΔV-volume domain neighboring the point $\boldsymbol{r}$. Since there is no magnetic particle outside the domain of magnetic materials, denoted Ω, M remains 0, owing to the randomness of atom orientations. Inside Ω, we have to analyze $\boldsymbol{M}$ by the principle of statistics. When an external magnetic field is applied, an atom will rotate and its magnetic moment will tend to (with a high probability) align with the direction of the magnetic field. Isotropic assumption states that this probability is the same no matter which direction the magnetic field orients. This is why the term *polarization* is also used to portray the magnetization. It should be noted that for a specific atom, the external magnetic field and the internal magnetic field induced by other atoms is non-distinguishable. These two fields jointly magnetize an atom as a whole.

Here is an example. For near-independent particles, such as those in ferrofluids, statistical physics states that

$$\overline{\boldsymbol{m}_i} = m_i \, L\left(\frac{m_i H}{k_\mathrm{B} T}\right) \frac{\boldsymbol{H}}{H}. \tag{42}$$

- $\overline{\boldsymbol{m}_i}$ is the expectation of $\boldsymbol{m}_i$ in equilibrium.
- k_B is the *Boltzmann constant*,
- T is the ambient temperature.
- $L(\cdot)$, which denotes the *Langevin function*, has the following form:

$$L(\alpha) = \coth \alpha - \frac{1}{\alpha}. \tag{43}$$

Because of the identity of atoms, the magnitude of each magnetic moment is identical. All the m_is are the same and all the $\overline{\boldsymbol{m}_i}$s within a particular infinitesimal domain are also equal. Let the former be m and the latter be $\overline{\boldsymbol{m}}(\boldsymbol{r})$. With n indicating the particle number density, constant in both time and space, we will acquire

$$\boldsymbol{M} = n\overline{\boldsymbol{m}} \tag{44}$$

$$= nm \, L\left(\frac{mH}{k_\mathrm{B} T}\right) \frac{\boldsymbol{H}}{H}. \tag{45}$$

Given constants $k_1 = nm$ and $k_2 = m/k_\mathrm{B}T$, Equation (44) can be rewritten as

$$M = k_1 \left(\coth k_2 H - \frac{1}{k_2 H}\right) \tag{46}$$

without regard to the direction.

If the intensity of the magnetic field is not that high, which suggests $k_2 H \ll 1$. Expanding the coth function in Equation (46), we will obtain

$$\begin{aligned} M &= k_1 \left[\frac{1}{k_2 H} + \frac{k_2 H}{3} + o\left((k_2 H)^3\right)\right] - \frac{k_1}{k_2 H} \\ &= \frac{k_1 k_2}{3} H + k_1 \, o\left((k_2 H)^3\right) \\ &\approx \frac{k_1 k_2}{3} H \end{aligned} \tag{47}$$

inside Ω, leading to linear assumption naturally. Let a new constant k equal to $k_1 k_2/3$. It is just the form we have seen in Equations (12c) and (12d).

A.3 Derivation of the Interfacial Helmholtz Force

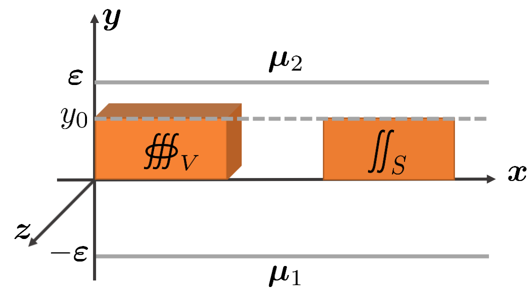

Fig. 19. A microelement around the interface, with $\varepsilon > 0$ as an infinitesimal. Since μ does not change perpendicular to y-axis, physical quantities are invariant in such a direction within this infinitesimal element. Therefore, this scene is reduced to a one-dimensional problem where the vector $\boldsymbol{r}$ can be replaced by the scalar y, with $\varphi(y) = y$ satisfied.

Given that there is an interface separating two materials with permeability μ_1 and μ_2 ($\mu_1 - \mu_2 = k\mu_0$) respectively (refer to Figure 19), we acquire

$$\mu(y) = \mu_1 + (\mu_2 - \mu_1)\theta(y). \tag{48}$$

By choosing the integration volume V and the integration surface S as illustrated in Figure 19, Maxwell's equations in magnetostatics derive

$$\begin{cases} \oiiint_V \nabla \cdot \boldsymbol{B} \, \mathrm{d}V = \oiint_{\partial V} \boldsymbol{B} \cdot \mathrm{d}\boldsymbol{S} = 0, & \text{(49a)} \\ \iint_S \nabla \times \boldsymbol{H} \cdot \mathrm{d}\boldsymbol{S} = \oint_{\partial S} \boldsymbol{H} \times \mathrm{d}\boldsymbol{r} = 0. & \text{(49b)} \end{cases}$$

With subscript 'n' and 't' indicating the normal component and the tangential component respectively, we define such functions:

$$\begin{cases} \boldsymbol{H}_\mathrm{t}(y_0) = \boldsymbol{H}|_{y=y_0} \times \hat{\boldsymbol{n}}, & \text{(50a)} \\ H_\mathrm{n}(y_0) = \boldsymbol{H}|_{y=y_0} \cdot \hat{\boldsymbol{n}}, & \text{(50b)} \\ \boldsymbol{B}_\mathrm{t}(y_0) = \boldsymbol{B}|_{y=y_0} \times \hat{\boldsymbol{n}}, & \text{(50c)} \\ B_\mathrm{n}(y_0) = \boldsymbol{B}|_{y=y_0} \cdot \hat{\boldsymbol{n}}. & \text{(50d)} \end{cases}$$

Here $\hat{\boldsymbol{n}}$ coincides with $\hat{\boldsymbol{y}}$. It is clear from Equation (49) that

$$\begin{cases} \boldsymbol{H}_\mathrm{t}(y_0) = \boldsymbol{H}_\mathrm{t}(0), & \text{(51a)} \\ B_\mathrm{n}(y_0) = B_\mathrm{n}(0), & \text{(51b)} \end{cases}$$

the latter of which can be further explained as

$$\mu(y_0) H_\mathrm{n}(y_0) = \mu(0) H_\mathrm{n}(0) = \frac{\mu_1 + \mu_2}{2} H_\mathrm{n}(0). \tag{52}$$

Taking the weak form of the Dirac delta function with ε as an infinitesimal, we do the following integral of Equation (29) over φ:

$$\begin{aligned} \boldsymbol{f}_{\mathrm{m}} &= \delta(\varphi)\int_{-\varepsilon}^{+\varepsilon}\frac{\mu_0}{2}kH^2\delta(\varphi)\hat{\boldsymbol{n}}\,\mathrm{d}\varphi \\ &= \frac{k\mu_0}{2}\hat{\boldsymbol{n}}\delta(\varphi)\int_{-\varepsilon}^{+\varepsilon}\left[\boldsymbol{H}_{\mathrm{t}}{}^2(0)+\frac{\mu^2(0)}{\mu^2(\varphi)}H_{\mathrm{n}}{}^2(0)\right]\delta(\varphi)\,\mathrm{d}\varphi \\ &= \frac{k\mu_0}{2}\hat{\boldsymbol{n}}\delta(\varphi)\left[\boldsymbol{H}_{\mathrm{t}}{}^2(0)+H_{\mathrm{n}}{}^2(0)\int_{-\varepsilon}^{+\varepsilon}\frac{\mu^2(0)}{\mu^2(\varphi)}\delta(\varphi)\,\mathrm{d}\varphi\right] \end{aligned} \tag{53}$$

in which

$$\begin{aligned} \int_{-\varepsilon}^{+\varepsilon}\frac{\mu^2(0)}{\mu^2(\varphi)}\delta(\varphi)\,\mathrm{d}\varphi &= \int_{-\varepsilon}^{+\varepsilon}\frac{\mu^2(0)}{[\mu_1+(\mu_2-\mu_1)\theta(\varphi)]^2}\frac{\mathrm{d}\theta(\varphi)}{\mathrm{d}\varphi}\,\mathrm{d}\varphi \\ &= \int_0^{+1}\frac{\mu^2(0)}{[\mu_1+(\mu_2-\mu_1)\theta]^2}\,\mathrm{d}\theta \\ &= -\frac{\mu^2(0)}{\mu_2-\mu_1}\left(\frac{1}{\mu_2}-\frac{1}{\mu_1}\right) \\ &= \frac{1}{1-\left(\frac{\mu_1-\mu_2}{\mu_1+\mu_2}\right)^2}. \end{aligned} \tag{54}$$

Substituting $\mu_2 = \mu_0$, $\mu_1 = (1+k)\mu_0$ into this integral, the rigorous formula of the Helmholtz force is

$$\boldsymbol{f}_{\mathrm{m}} = \frac{\mu_0}{2}k\left[H^2+\frac{k^2}{4k+4}(\boldsymbol{H}\cdot\hat{\boldsymbol{n}})^2\right]\delta(\varphi(\boldsymbol{r}))\hat{\boldsymbol{n}}. \tag{55}$$

Considering that

$$\begin{cases} \boldsymbol{H}_1 = \lim\limits_{\varepsilon\to 0}\boldsymbol{H}|_{y=-\varepsilon}, & (56\mathrm{a}) \\ \boldsymbol{H}_2 = \lim\limits_{\varepsilon\to 0}\boldsymbol{H}|_{y=+\varepsilon}, & (56\mathrm{b}) \end{cases}$$

it is not hard to prove that $\boldsymbol{H}$ on the interface is a weighted average of $\boldsymbol{H}_1$ and $\boldsymbol{H}_2$, just as Equation (21) shows.